

Energy, Environmental, and Catalysis Applications

**Macroscale and Nanoscale Photoelectrochemical Behavior of p-Type Si(111) Covered by a Single Layer of Graphene or Hexagonal Boron Nitride**

Annelise Christine Thompson, Burton H. Simpson, and Nathan S. Lewis

*ACS Appl. Mater. Interfaces*, **Just Accepted Manuscript** • DOI: 10.1021/acsami.9b21134 • Publication Date (Web): 10 Feb 2020Downloaded from [pubs.acs.org](https://pubs.acs.org) on February 10, 2020**Just Accepted**

“Just Accepted” manuscripts have been peer-reviewed and accepted for publication. They are posted online prior to technical editing, formatting for publication and author proofing. The American Chemical Society provides “Just Accepted” as a service to the research community to expedite the dissemination of scientific material as soon as possible after acceptance. “Just Accepted” manuscripts appear in full in PDF format accompanied by an HTML abstract. “Just Accepted” manuscripts have been fully peer reviewed, but should not be considered the official version of record. They are citable by the Digital Object Identifier (DOI®). “Just Accepted” is an optional service offered to authors. Therefore, the “Just Accepted” Web site may not include all articles that will be published in the journal. After a manuscript is technically edited and formatted, it will be removed from the “Just Accepted” Web site and published as an ASAP article. Note that technical editing may introduce minor changes to the manuscript text and/or graphics which could affect content, and all legal disclaimers and ethical guidelines that apply to the journal pertain. ACS cannot be held responsible for errors or consequences arising from the use of information contained in these “Just Accepted” manuscripts.

# Macroscale and Nanoscale Photoelectrochemical Behavior of p-Type Si(111) Covered by a Single Layer of Graphene or Hexagonal Boron Nitride

*Annelise C. Thompson<sup>‡</sup>, Burton H. Simpson<sup>‡</sup>, and Nathan S. Lewis<sup>\*</sup>.*

Division of Chemistry and Chemical Engineering, California Institute of Technology, Pasadena, CA, 91125, United States

KEYWORDS: 2D material, graphene, hexagonal boron nitride, photoelectrochemistry, semiconductor/liquid junction, scanning electrochemical cell microscopy

ABSTRACT: Two-dimensional (2D) materials may enable a general approach to introduction of a dipole at a semiconductor surface as well as control over other properties of the double layer at a semiconductor/liquid interface. Vastly different properties can be found in the 2D materials currently studied due in part to the range of the distribution of density-of-states. In this work, the open-circuit voltage ( $V_{oc}$ ) of p-Si-H, p-Si/Gr (graphene) and p-Si/h-BN (hexagonal boron nitride) in contact with a series of one-electron outer-sphere redox couples was investigated by macroscale measurements as well as by scanning electrochemical cell microscopy (SECCM). The band gaps of Gr and h-BN (0-5.97 eV) encompass the wide range of band gaps for 2D materials, so these interfaces (p-Si/Gr and p-Si/h-BN) serve as useful references to understand the behavior of 2D

1  
2  
3 materials more generally. The value of  $V_{oc}$  shifted with respect to the effective potential of the  
4 contacting solution, with slopes ( $\Delta V_{oc}/\Delta E_{Eff}$ ) of -0.27 and -0.38 for p-Si/Gr and p-Si/h-BN  
5 respectively, indicating that band bending at the p-Si/h-BN and p-Si/Gr interfaces responds at least  
6 partially to changes in the electrochemical potential of the contacting liquid electrolyte.  
7  
8 Additionally, SECCM is shown to be an effective method to interrogate the nanoscale  
9 photoelectrochemical behavior of an interface, showing little spatial variance over scales  
10 exceeding the grain size of the CVD-grown 2D materials in this work. The measurements  
11 demonstrated that the polycrystalline nature of the 2D materials had little effect on the results and  
12 confirmed that the macroscale measurements reflected the junction behavior at the nanoscale.  
13  
14  
15  
16  
17  
18  
19  
20  
21  
22  
23  
24

## 25 **Introduction**

26  
27  
28 Covalent functionalization of semiconductor surfaces is an established method for manipulating  
29 the energetics of semiconductor interfaces. Development of the chemistry needed for such  
30 functionalization can be time-consuming, and this strategy is not easily translated between  
31 materials without extensive work to develop and characterize new reactions. Coating  
32 semiconductors such as n-type silicon (n-Si) with a monolayer of graphene (Gr) or fluorinated  
33 graphene (F-Gr) represents a potentially general strategy for protection of semiconductor  
34 surfaces against oxidation during photoanodic operation in aqueous solution as well as for  
35 manipulation of the band-edge positions and energetics of the semiconductor/liquid interface.<sup>1-2</sup>  
36  
37 The open-circuit voltage ( $V_{oc}$ ) of these electrodes shifts in contact with a series of nonaqueous  
38 redox couples of varying potentials, indicating a lack of Fermi-level pinning even though the  
39 Fermi level ( $E_F$ ) of monolayer Gr is similar to that of graphite (-4.6 eV vs. vacuum), and lies  
40 mid-gap relative to the silicon band-edge positions.<sup>3</sup> With the recent expansion of the number  
41  
42  
43  
44  
45  
46  
47  
48  
49  
50  
51  
52  
53  
54  
55  
56  
57  
58  
59  
60

1  
2  
3 and classes of two-dimensional (2D) materials that can be isolated, covering semiconductors  
4  
5 with 2D materials may represent an effective method to manipulate, as determined by the  
6  
7 electronic states in the 2D material, the interfacial energetics and chemistry of semiconductor  
8  
9 surfaces.  
10

11  
12  
13 Further understanding the effects of the density of states of a 2D material on an interface is key to  
14  
15 the successful integration of these materials into devices. Many of the extraordinary properties  
16  
17 that have made Gr so well studied arise from the existence of a Dirac point in the density of states.<sup>4</sup>  
18  
19 The electronic structure of Gr also results in the presence of a finite number of surface states within  
20  
21 the band gap of silicon. These states contribute to the formation of a rectifying potential-dependent  
22  
23 barrier height ( $\phi_B$ ) in contact with both n-type and p-type Si, unlike the potential-independent  
24  
25 barrier heights of many semiconductor-electrolyte and semiconductor-metal interfaces<sup>5</sup>. However,  
26  
27 these states, and the resulting dependence of the barrier height on potential, can also attenuate the  
28  
29 barrier height of fabricated devices by partially or fully pinning the interface energetics.<sup>1, 6-7</sup> In  
30  
31 contrast, hexagonal boron nitride (h-BN), a structural analogue of Gr consisting of an alternating  
32  
33 lattice of boron and nitrogen atoms, is primarily used as an inert protective layer in 2D material  
34  
35 heterostructures. h-BN is an insulator with a band gap of 5.97 eV.<sup>8</sup> Gr has found widespread  
36  
37 application in photoelectrochemical cells, including as a transparent electrode and catalyst  
38  
39 support,<sup>9</sup> while h-BN has been demonstrated to be an effective tunnel barrier even at a monolayer<sup>10</sup>  
40  
41 and enhances the performance of Gr-on-Si Schottky junction solar cells.<sup>11</sup> h-BN should not  
42  
43 introduce states within the band gap of Si and thus should provide a useful endpoint for comparison  
44  
45 with Gr, because the band gaps of most 2D materials fall between the range presented by these  
46  
47 two materials (0 eV-5.97 eV). Moreover, the behavior of each at an interface should be reflective  
48  
49 of the density of states within the band gap of Si.  
50  
51  
52  
53  
54  
55  
56  
57  
58  
59  
60

1  
2  
3 Substantial discrepancies have been reported between barrier heights of Si/2D/metal  
4 interfaces. An ohmic contact has been observed for an n-Si/Gr/Ni junction using nanoscale AFM  
5 measurements (contact size diameter  $\sim 40\text{-}50\text{ nm}$ ),<sup>12</sup> whereas macroscale measurements (contact  
6 size diameter  $\sim 500\text{ }\mu\text{m}$ ) of the same interface have been reported to exhibit strongly rectifying  
7 behavior.<sup>7</sup> Additional work has shown that the  $\phi_B$  of an n-Si/2D/metal interface is fully pinned  
8 with respect to the work function of metal, across a range of contact sizes (60 nm-100  $\mu\text{m}$ ).<sup>6</sup> Both  
9 the size of the metal contact and the measurement technique have an effect on the observed  
10 behavior of Si/2D/metal interfaces. In these Si/2D/metal interfaces, simulations have indicated that  
11 the distance between the 2D material and metal top contact, and hybridization of that metal with  
12 the 2D material in question through physisorption or chemisorption, decrease the resulting  $\phi_B$  of  
13 the interface.<sup>13-14</sup> This hybridization causes an analogous, but fully 2D material heterojunction  
14 formed from MoS<sub>2</sub>/Gr/metal to exhibit lower contact resistances when a purposefully defective Gr  
15 layer is inserted at the interface, allowing increased interactions between the Gr and metal.<sup>15</sup> This  
16 variance in observed behavior at Si/2D/metal interfaces, and the dependence of contact resistance  
17 on defects, collectively complicate formulation of a complete understanding electron-transfer at  
18 the interface especially as more complex stacks are constructed. Techniques that rely on formation  
19 of metallic top contacts do not readily facilitate resolution of differences in spatial heterogeneity  
20 across an interface nor provide results that are readily compared with macroscale measurements.  
21 Thus, to systematically understand how the properties of the semiconductor/2D interface vary,  
22 devices with uniform, nondestructive top contacts, such those formed in a liquid junction cell, can  
23 be used to avoid the substantial effect of the 2D material/metal interaction on the  
24 semiconductor/2D/contact interface. An understanding of the role of Gr and h-BN at a  
25 semiconductor/liquid junction, which affords precise control over the potential of the interface,  
26  
27  
28  
29  
30  
31  
32  
33  
34  
35  
36  
37  
38  
39  
40  
41  
42  
43  
44  
45  
46  
47  
48  
49  
50  
51  
52  
53  
54  
55  
56  
57  
58  
59  
60

1  
2  
3 will inform further work on the trends expected from more complex semiconductor/stacked 2D  
4 material heterojunctions.  
5  
6

7  
8  
9 Ideal interfaces could be produced using exclusively pristine, single crystals of the 2D material,  
10 but such samples are technologically not yet available for measurements on macroscale electrodes.  
11  
12 Single crystals of 2D materials can be obtained through mechanical exfoliation of layered  
13 materials, but these methods do not produce single crystals of a size large enough to cover even  
14 laboratory-scale ( $\sim 1 \text{ cm}^2$ ) photoelectrodes. Consequently, in our work, 2D materials grown by  
15 chemical-vapor deposition (CVD) have been used to produce large ( $>1 \text{ cm}^2$ ) area samples. CVD-  
16 grown 2D materials currently represent the materials most similar to those easily used in both  
17 general research and industrial device fabrication. However, CVD-grown Gr and h-BN are both  
18 polycrystalline materials that inherently contain grain boundaries and defects. The distinct  
19 differences between the electronic structure of the pristine material and the defective sites may  
20 locally impact the energetics at the semiconductor/2D/liquid junction and thus also influence the  
21 macroscale behavior of such systems.<sup>16</sup> To address this issue, scanning electrochemical cell  
22 microscopy (SECCM) has been used herein to supplement macroscale understanding of the  
23 junction energetics with submicron spatial resolution, which is a length scale sufficient to  
24 interrogate the behavior within a grain of the CVD-grown 2D materials studied in our work.  
25  
26  
27  
28  
29  
30  
31  
32  
33  
34  
35  
36  
37  
38  
39  
40  
41  
42  
43

44 SECCM is a scanning probe microscopy technique introduced by Unwin in 2010 that utilizes an  
45 electrolyte-filled glass nanopipette as the probe.<sup>17</sup> The counter and reference electrodes of an  
46 electrochemical cell are housed within this pipette and connected to a potentiostat. Using a  
47 micropositioner, the opening of the pipette is brought close to a surface being operated as the  
48 working electrode, until a nanoscale liquid junction is formed between the pipette and the surface,  
49 completing the circuit for the electrochemical cell. The probe is then operated as an  
50  
51  
52  
53  
54  
55  
56  
57  
58  
59  
60

1  
2  
3 electrochemical cell with a working electrode area defined by the size of the liquid junction.  
4  
5 SECCM allows standard electrochemical techniques to be performed with a high degree of spatial  
6  
7 resolution,<sup>18-19</sup> and has previously been used in photoelectrochemical systems to measure and  
8  
9 resolve photocurrents on heterogeneous surfaces.<sup>20</sup> In addition to enabling spatially resolved  
10  
11 electrochemistry, the small surface area of the working electrode in contact with electrolyte makes  
12  
13 SECCM especially useful for samples that may readily degrade or change structure under  
14  
15 electrochemical operation, because a location can be tested without affecting the remainder of the  
16  
17 sample.  
18  
19  
20  
21

22  
23 Scanning electrochemical microscopy (SECM) and SECCM have previously revealed differences  
24  
25 between the macroscale and nanoscale electrochemistry of 2D materials. CVD-grown Gr often  
26  
27 exhibits lower interfacial electron-transfer rate constants than graphite, the bulk equivalent of Gr.  
28  
29 SECM studies using nanoelectrodes have indicated that this difference is specific to Gr electrodes  
30  
31 that are supported by polymethyl methacrylate (PMMA), as is commonly practiced in fabrication  
32  
33 of Gr devices.<sup>21</sup> In contrast, polystyrene-supported electrodes had electron-transfer rates that were  
34  
35 similar to those of graphite. These techniques have also been used to probe heterogeneity in  
36  
37 electrochemical reactivity across the surfaces of 2D materials. Gr edges at mechanically induced  
38  
39 defects exhibit interfacial electron-transfer rate constants nearly an order of magnitude higher than  
40  
41 rate constants measured for the Gr basal plane.<sup>22</sup> Notably, the spatial resolution of the electrodes  
42  
43 used in that study would result in contributions to the observed kinetics from both basal plane and  
44  
45 edge sites. SECCM studies have probed the impact of the number of Gr layers on the  
46  
47 electrochemical kinetics, and concluded that the reactivity is largely determined by the density of  
48  
49 states, with exposed edges showing especially high reactivity.<sup>19</sup> Similarly increased activity has  
50  
51  
52  
53  
54  
55  
56  
57  
58  
59  
60

1  
2  
3 been observed at the edges of exfoliated MoS<sub>2</sub> nanoflakes using scanning photocurrent  
4  
5 microscopy.<sup>23</sup>  
6

7  
8  
9 For a complete understanding of 2D material/semiconductor interfaces, the effect of the density-  
10  
11 of-states of a 2D material on the resulting junction must be systematically understood. We have  
12  
13 used macroscale photoelectrochemical measurements to probe the effect of 2D materials that have  
14  
15 substantially different mutual distributions of their density-of-states by comparing the  
16  
17 photoelectrochemical behavior of Gr and h-BN covered p-type silicon (p-Si) photoelectrodes to  
18  
19 H-terminated p-Si (111) surfaces. Inserting two-dimensional materials at the semiconductor/liquid  
20  
21 junction are shown to have a measurable impact on junction energetics through the equilibration  
22  
23 of the Fermi levels of the semiconductor and the 2D material, depending on the density of states  
24  
25 of the interstitial 2D material. Supporting measurements on the nanoscale with SECCM probes  
26  
27 that are far smaller than the grain size of the 2D materials used in this study corroborates the trends  
28  
29 of the p-Si/2D junctions recorded on the macroscale without substantial contributions from grain  
30  
31 boundaries. By establishing the macroscale behavior of conductive and insulating 2D materials as  
32  
33 interstitial layers and developing liquid probes to interrogate junction energetics on the macroscale,  
34  
35 this study develops the fundamental understanding needed to successfully integrate 2D materials  
36  
37 into photoelectrochemical devices.  
38  
39  
40  
41  
42  
43

## 44 **Methods**

### 45 *Materials*

46  
47  
48 Acetonitrile (Dri-Solv, 99.9%) was purchased from Fisher Scientific and used as received. Lithium  
49  
50 perchlorate (LiClO<sub>4</sub>, 99.99%, battery grade) was purchased from Sigma Aldrich and used as  
51  
52 received.  
53  
54  
55  
56  
57  
58  
59  
60



1  
2  
3 Ferrocene ( $\text{Cp}_2\text{Fe}^0$ ), dimethylferrocene ( $\text{Me}_2\text{Cp}_2\text{Fe}^0$ ), decamethylferrocene ( $\text{Cp}^*_2\text{Fe}^0$ ) nickelocene  
4 ( $\text{Cp}_2\text{Ni}^0$ ), and cobaltocene ( $\text{Cp}_2\text{Co}^0$ ) were all purchased from Sigma-Aldrich and purified by  
5  
6 sublimation. Octamethylnickelocene ( $\text{Me}_8\text{Cp}_2\text{Ni}^0$ ) was purchased from Sigma-Aldrich and used  
7  
8 as received. Cobaltocenium ( $\text{Cp}_2\text{Co}^+$ ) hexafluorophosphate (Sigma-Aldrich, 98%) was  
9  
10 recrystallized from ethanol. Decamethylcobaltocenium ( $\text{Cp}^*_2\text{Co}^+$ ) hexafluorophosphate (Sigma-  
11  
12 Aldrich, 98%) was recrystallized from  $\text{CH}_3\text{CN}$  using ethanol as an antisolvent. Methyl viologen  
13  
14 hexafluorophosphate ( $\text{MV}(\text{PF}_6)_2$ ) was prepared by metathesis of methyl viologen dichloride  
15  
16 (Sigma-Aldrich, 98%) with ammonium hexafluorophosphate (Sigma-Aldrich, 99.98%) in water,  
17  
18 and was recrystallized from ethanol.  
19  
20  
21  
22  
23

24  
25 All chemicals were stored in a  $\text{N}_2(\text{g})$ -filled flush box that contained  $<3$  ppm  $\text{O}_2(\text{g})$ . Electrolyte  
26  
27 solutions were prepared in the flush box using  $\text{CH}_3\text{CN}$  with 0.50 M  $\text{LiClO}_4$  as the supporting  
28  
29 electrolyte. Except for  $\text{Cp}^*_2\text{Fe}^0$  and  $\text{MV}^{2+}$ , which had limited solubility, all of the redox couples  
30  
31 were prepared at initial concentrations of  $\sim 10$  mM of the available species. Bulk electrolysis was  
32  
33 used to generate the reduced species  $\text{Me}_8\text{Cp}_2\text{Ni}$ ,  $\text{MV}^+$ , and  $\text{Cp}^*_2\text{Co}$ , as well as all of the oxidized  
34  
35 forms of the metallocenes except  $\text{Cp}_2\text{Co}^+$ .  
36  
37  
38

39  
40 For electrochemical measurements, double-side polished, boron-doped, p-type Si(111) wafers (0.3  
41  
42  $\Omega$  cm resistivity, with an acceptor concentration,  $N_A = 7 \times 10^{16} \text{ cm}^{-3}$ ) were obtained from Addison  
43  
44 Engineering, Inc. Immediately before transfer of Gr or h-BN, the native oxide on the p-Si wafer  
45  
46 pieces was etched using improved buffered HF (BHF, Transene). BHF was also used to clean bare  
47  
48 p-Si electrodes immediately before electrochemical testing.  
49  
50

51  
52 CVD-grown monolayer Gr on Cu (Cu/Gr) and CVD-grown monolayer h-BN on Cu (Cu/h-BN)  
53  
54 were purchased from Advanced Chemical Supplier Materials (Medford, MA). Grains of Gr from  
55  
56  
57  
58  
59  
60

1  
2  
3 this source are  $\sim 50 \mu\text{m}$  in diameter, as reported by the manufacturer, while grains of h-BN from  
4  
5 this source are  $\sim 4 \mu\text{m}$  in diameter.  
6  
7

### 8 *Electrode fabrication*

9  
10  
11 Ohmic back contacts to the p-type Si wafers were formed by evaporation of 100 nm of Au (Labline  
12  
13 Electron Beam Evaporator, Kurt J. Lesker) followed by an anneal at 350 °C under forming gas  
14  
15 ( $\text{H}_2(\text{g}):\text{N}_2(\text{g})$  v:v 5:95). Wafer pieces used for SECCM measurements were additionally  
16  
17 lithographically patterned with registry marks, to track the location of the electrochemical  
18  
19 measurements and ensure that data were collected on intact portions of the 2D material monolayer.  
20  
21  
22

23  
24 The h-BN used in this study was grown on Cu, analogously to the Gr, hence electrodes for both  
25  
26 2D materials were made by a similar process. The methods for the Gr electrodes are described in  
27  
28 detail below. To make the coated electrodes, a strip of Cu covered by monolayer Gr (Cu/Gr) was  
29  
30 coated with a supporting polymer layer of 495K A4 polymethyl methacrylate (PMMA,  
31  
32 MicroChem) at 3000 rpm for 60 s. The resulting stack (Cu/Gr/PMMA) was then cured for 5 min  
33  
34 at 120 °C. Smaller pieces, which matched the desired size of the electrodes being fabricated, were  
35  
36 cut and etched in a  $\text{FeCl}_3$  etch solution (Copper etch, Transene) until the Cu disappeared by visual  
37  
38 inspection, generally requiring  $\sim 1.5$  h. This Cu-free piece (Gr/PMMA) was transferred to a  $\geq 18.2$   
39  
40  $\text{M}\Omega\text{-cm}$  resistivity  $\text{H}_2\text{O}$  bath for 1 h before transfer to a second clean  $\text{H}_2\text{O}$  bath into which the  
41  
42 sample was immersed for 12 h. After transfer to a final fresh  $\text{H}_2\text{O}$  bath, the stack was pulled onto  
43  
44 a p-Si wafer piece that had been etched with improved buffered HF, dried thoroughly using a  
45  
46 gentle stream of  $\text{N}_2(\text{g})$ , and heated to 80 °C for 10 min to allow the PMMA layer to reflow. The  
47  
48 substrate was then rinsed in acetone for 10 min before being annealed for 2 h at 350 °C in a  
49  
50  
51  
52  
53  
54  
55  
56  
57  
58  
59  
60

1  
2  
3 reducing atmosphere ( $\text{H}_2(\text{g}):\text{Ar}(\text{g})$  v:v 5:95), to remove any residual PMMA from the transfer  
4 process.  
5  
6

7  
8 The p-Si/Gr stack was attached to a Cu wire using a Ga-In eutectic alloy and high-purity Ag paint  
9 (SPI Supplies, West Chester, Pennsylvania). The back of the electrode was covered with a layer  
10 of clear nail polish to minimize leakage of the Ga-In eutectic. The sample was then sealed to a  
11 Pyrex tube with a layer of Loctite 9460 Hysol epoxy and cured overnight. The area of the resulting  
12 electrode was measured using ImageJ software for analysis of optical images of each electrode.  
13  
14  
15  
16  
17  
18

19  
20 For the macroscale measurements, a set of control electrodes ( $\text{p-SiO}_x$ ), which were exposed to the  
21 same transfer process without the introduction of a 2D material, were made by otherwise nominally  
22 identical processes to those used to make the p-Si/Gr and p-Si/h-BN electrodes described above.  
23  
24  
25

26 In brief, a layer of PMMA was spun onto a bare Cu foil to generate a Cu/PMMA stack. This stack  
27 was processed identically to the Cu/Gr/PMMA stacks, yielding p-Si-H samples that did not  
28 contain a 2D overlayer. These samples will be referred to as  $\text{p-SiO}_x$ , or blank electrodes, as the  
29 processing and annealing steps generated a small amount of silicon oxide on the surface, in contrast  
30 to the p-Si-H electrodes, which immediately prior to testing were etched with improved buffered  
31 HF to remove any residual oxide.  
32  
33  
34  
35  
36  
37  
38  
39  
40  
41

42 SECCM samples were made analogously to the bulk process above, with the Gr and h-BN samples  
43 transferred to the same p-Si wafer chip to ensure uniformity between the two materials. After  
44 annealing, the sample was attached through the back contact to a custom SECCM stage for  
45 analysis.  
46  
47  
48  
49  
50  
51  
52  
53  
54  
55  
56  
57  
58  
59  
60

1  
2  
3 For Hall measurements, samples were prepared using the methods described above to transfer Gr  
4 to p-Si that was coated with a 300 nm thermal oxide. Au top contacts and a thin Ti adhesion layer  
5 were deposited by e-beam evaporation.  
6  
7

8  
9  
10  
11 For UV/Vis measurements, samples were prepared using the methods described above to transfer  
12 Gr or h-BN to a quartz slide before processing and annealing as before.  
13  
14

15  
16 For surface recombination velocity (SRV) measurements, samples were prepared as above and  
17 transferred to floatzone-grown, double-side polished Si wafers that were not intentionally doped,  
18 had a resistivity of 20 k $\Omega$  cm, and were 300  $\pm$  25  $\mu$ m thick (Semiconductor Processing Co.) before  
19 processing and annealing as before.  
20  
21  
22  
23  
24

### 25 26 *Electrochemical Methods*

27  
28  
29  
30 Bulk electrolysis was performed in a four-necked round-bottom flask inside a N<sub>2</sub>(g)-purged flush  
31 box that contained <3 ppm O<sub>2</sub>(g). The working and counter electrodes were Pt meshes, and the  
32 reference electrode was a Pt-polypyrrole (Pt-PPy) electrode prepared in a CH<sub>3</sub>CN–0.50 M LiClO<sub>4</sub>  
33 solution.<sup>24</sup> The reference and counter electrodes were each contained in separate compartments  
34 constructed from borosilicate tubing, with a Vycor porous glass frit attached to the end of the glass  
35 tubing by use of Teflon heat-shrink tubing. Each compartment was filled with CH<sub>3</sub>CN–0.50 M  
36 LiClO<sub>4</sub>. The bulk electrolysis was monitored by cyclic voltammetry using a 12.5  $\mu$ m radius Au  
37 ultramicroelectrode.  
38  
39  
40  
41  
42  
43  
44  
45  
46  
47  
48

49 All macroscale measurements were performed inside an Ar-filled dry box with <0.5 ppm O<sub>2</sub>(g),  
50 with leads connected externally to a SP-200 Biologic potentiostat. The reference electrode was Pt-  
51 PPy, deposited from a 10 mM solution of pyrrole in CH<sub>3</sub>CN–0.50 M LiClO<sub>4</sub>.<sup>24</sup> The reference  
52  
53  
54  
55  
56  
57  
58  
59  
60

1  
2  
3 electrode was remade for use with each redox couple, and consistently produced a stable potential  
4 of  $\sim +0.20$  V vs. Ag/AgCl. For each redox couple, cyclic voltammograms on p-Si-H, p-SiO<sub>x</sub>, p-  
5 Si/Gr, and p-Si/h-BN were recorded at a 50 mV s<sup>-1</sup> scan rate either under illumination or in the  
6 dark. The  $V_{oc}$  was measured multiple times for each electrode, although the duration of the  
7 measurements was adjusted for different redox couples to allow ample time for  $V_{oc}$  to stabilize.  
8  
9

10  
11  
12  
13  
14  
15  
16 Pipettes for SECCM were prepared using a Sutter Instruments P-2000 laser puller. Quartz theta  
17 capillaries (1.2 mm outer diameter, 0.9 mm inner diameter; Sutter Instruments) were first cleaned  
18 with acetone and methanol, and were then pulled to create pipettes having openings between 50-  
19 500 nm in radius. The pipettes were then silanized with chlorotrimethylsilane to create a  
20 hydrophobic surface.<sup>25</sup> Pipettes were filled with electrolyte solutions using a glass syringe and a  
21 stainless-steel needle.  
22  
23  
24  
25  
26  
27  
28  
29

30  
31 All SECCM measurements were performed using a CHI 920D potentiostat inside a N<sub>2</sub>(g)-purged  
32 flush box that contained < 3 ppm O<sub>2</sub>(g). The counter and reference electrodes were 0.2 mm  
33 diameter Pt wires, each on opposite sides of the theta pipette, and the p-Si photoelectrode was the  
34 working electrode. Prior to approaching the surface, an endoscope was used to position the  
35 pipettes to within 20 μm of the desired location. As pipettes were approached to the surface, the  
36 substrate was then biased positive with respect to the reference electrode. Movement automatically  
37 stopped when the potentiostat detected the current spike that occurred when a liquid junction  
38 formed. The size of the liquid junction was approximated from the anodic  $i_{ss}$  of the redox couple  
39 as measured from a linear sweep voltammogram taken in the dark using the equation  $i_{ss} = 4nFaDc^*$ ,  
40 where  $n$  is the number of electrons transferred per oxidation,  $F$  is Faraday's constant,  $a$  is the radius  
41 of the tip,  $D$  is the diffusion coefficient of the redox species, and  $c^*$  is the bulk concentration of the  
42 redox species. Only measurements taken using junctions with radii of a <200 nm were included in  
43  
44  
45  
46  
47  
48  
49  
50  
51  
52  
53  
54  
55  
56  
57  
58  
59  
60

1  
2  
3 this study, as larger junctions were unstable. Illumination for photoelectrochemical SECCM  
4 experiments was provided at a 45° angle by a fiber optic attached to an ELH-type W-halogen lamp  
5 with a dichroic rear reflector, with the entire optical train and light source located inside the flush  
6 box. The measured illumination intensity was equivalent to 100 mW cm<sup>-2</sup> of Air Mass 1.5 sunlight  
7 as measured by a NIST-calibrated photodiode. As in the macroscale measurements, cyclic  
8 voltammograms at each location using each redox couple were recorded at a 50 mV s<sup>-1</sup> scan rate  
9 either in the presence or absence of illumination. Open-circuit voltage measurement times were  
10 adjusted for different redox couples and locations to allow sufficient time for  $V_{oc}$  to stabilize in  
11 each case.  
12  
13  
14  
15  
16  
17  
18  
19  
20  
21  
22  
23

### 24 *Instruments*

25  
26  
27  
28 XPS data were collected at 1×10<sup>-9</sup> Torr using a Kratos AXIS Ultra DLD with a magnetic immersion  
29 lens that consisted of a spherical mirror and concentric hemispherical analyzers with a delay-line  
30 detector (DLD). An Al K $\alpha$  (1.486 KeV) monochromatic source was used for X-ray excitation.  
31 Ejected electrons were collected at a 90° angle from the horizontal. The CASA XPS software  
32 package v 2.3.16 was used to analyze the collected data.  
33  
34  
35  
36  
37  
38  
39

40  
41 Carrier mobilities were obtained using an H-50 MMR Hall Measurement System. Raman spectra  
42 were collected with a Renishaw Raman microscope at a wavelength of 532 nm through an  
43 objective with numerical aperture of 0.75. The laser power was ~3 mW. UV/Vis transmission  
44 spectra were collected with a Cary 5000 absorption spectrometer equipped with an external DRA  
45 1800 attachment. The data were automatically zero/baseline corrected by the instrument before  
46 any additional processing was performed. Surface recombination velocity (S) measurements were  
47 collected with a contactless microwave conductivity apparatus, which used a 20 ns laser pulse at  
48  
49  
50  
51  
52  
53  
54  
55  
56  
57  
58  
59  
60

1  
2  
3 905 nm generated by an OSRAM laser diode and an ETX-10A-93 driver to form electron–hole  
4  
5 pairs. The charge-carrier lifetime was determined by monitoring the change in reflected microwave  
6  
7 intensity using a PIN diode connected to an oscilloscope. The data was collected using a custom  
8  
9 LabView program. All photoconductivity decay curves were averages of 16 consecutive decays.  
10  
11

## 12 13 **Results**

### 14 15 16 *Characterization*

17  
18  
19 X-ray photoelectron spectroscopy, Raman spectroscopy, and UV/vis spectroscopy collectively  
20  
21 indicated that the polycrystalline monolayers used in this work were intact over areas exceeding  
22  
23 the area expected for a single grain ( $\sim 25\text{-}2500\ \mu\text{m}^2$ ) and displayed the expected electrical  
24  
25 characteristics for Gr and h-BN (Figure S1-S6), respectively. The h-BN monolayers had a band  
26  
27 gap of 6.07 eV and transmitted  $\sim 100\%$  of the light between 250-1200 nm in wavelength as  
28  
29 determined by UV/Vis spectroscopy. Gr had no band gap and transmitted  $\sim 97\%$  of light over the  
30  
31 same region. Measurements of the Hall mobility of Gr were collected for four different samples  
32  
33 with electrodes in a van der Pauw configuration, and yielded an average value of  $9.7 \times 10^2\ \text{cm}^2\ \text{V}^{-1}$   
34  
35  $\text{s}^{-1}$ , which falls within the range expected for monolayer polycrystalline Gr transferred using a wet  
36  
37 chemical method ( $500\text{-}10,000\ \text{cm}^2/\text{V}\cdot\text{s}$ ).<sup>26-28</sup> Ultraviolet photoelectron spectroscopy (UPS) was  
38  
39 used to measure the band positions and to determine any effects of the fabrication process of each  
40  
41 type of sample (Table S1). The p-Si–H samples exhibited a work function of  $4.40 \pm 0.07\ \text{eV}$  whereas  
42  
43 p-SiO<sub>x</sub>, p-Si/Gr, and p-Si/h-BN had work functions on average of  $4.92 \pm 0.0017\ \text{eV}$ ,  $4.73 \pm 0.007$   
44  
45 eV, and  $4.77 \pm 0.006\ \text{eV}$ , respectively.  
46  
47  
48  
49  
50  
51

### 52 53 *Electrochemistry*

1  
2  
3 Figure 1 presents the representative macroscale current density versus potential ( $J$ - $E$ ) behavior for  
4 p-Si-H, p-SiO<sub>x</sub>, p-Si/Gr, and p-Si/h-BN electrodes, respectively, in the dark and under 100 mW  
5 cm<sup>-2</sup> of ELH-type W-halogen simulated solar illumination in CH<sub>3</sub>CN–0.50 M lithium perchlorate  
6 solutions containing either ferrocene<sup>+0</sup> or cobaltocene<sup>+0</sup>. The samples referred to as p-SiO<sub>x</sub>, or  
7 “blank” electrodes, in reference to the small amount of oxide grown on the surface during  
8 fabrication (*vide supra*), are also included in the macroscale measurements to show the behavior  
9 of a p-Si-H electrode when subjected to nominally the same processing steps as the p-Si/Gr and  
10 p-Si/h-BN electrodes in the absence of transferring a 2D overlayer to the surface (Figure S7). For  
11 macroscale electrodes, the bare p-Si-H and p-SiO<sub>x</sub> electrodes exhibited rectifying behavior toward  
12 both redox couples, as indicated by increased cathodic photocurrent under increasing negative  
13 potentials (i.e. increasing reverse bias). As expected from the relative position of the Fermi level  
14 of p-Si with respect to the redox couples shown, the shift in the open-circuit voltage,  $V_{oc}$ , measured  
15 relative to the Nernstian potential of the solution,  $E(A/A^-)$ , for these electrodes under illumination  
16 was larger in contact with Cp<sub>2</sub>Co<sup>+0</sup>, which has a more negative effective redox potential,  $E_{eff}$ , (see  
17 SI and Ref. 31 for calculation of the concentration-corrected effective redox potential,  $E_{eff}$ , relative  
18 to the Nernstian potential of the solution,  $E(A/A^-)$ ), than for Cp<sub>2</sub>Fe<sup>+0</sup>. In contact with Cp<sub>2</sub>Fe<sup>+0</sup>, p-  
19 Si/h-BN electrodes exhibited minimal rectification and displayed substantial currents under  
20 reverse bias in the dark. In contact with Cp<sub>2</sub>Co<sup>+0</sup>, these electrodes showed strong rectification,  
21 with only minimal dark current and a large photocurrent. In contrast, the p-Si/Gr samples exhibited  
22 ohmic behavior in the Cp<sub>2</sub>Fe<sup>+0</sup> solution and moderately rectifying behavior in contact with the  
23 Cp<sub>2</sub>Co<sup>+0</sup> solution, as shown by the rapid increase in currents under forward bias for both of these  
24 sample types in the dark.  
25  
26  
27  
28  
29  
30  
31  
32  
33  
34  
35  
36  
37  
38  
39  
40  
41  
42  
43  
44  
45  
46  
47  
48  
49  
50  
51  
52  
53  
54  
55  
56  
57  
58  
59  
60



1  
2  
3 Similar was observed behavior for all samples by SECCM, except for the p-Si/Gr interface (Figure  
4 2). The macroscale measurements are shown as current density versus potential, whereas due to  
5 effect of pipette tip size on resulting current density, the SECCM data are displayed using current  
6 normalized to the transport-limited steady-state current ( $i/i_{ss}$ ) observed during cathodic operation  
7 under illumination.<sup>29-30</sup>  
8  
9  
10  
11  
12  
13

14  
15 During macroscale testing, six replicate photoelectrodes were tested for each redox couple.  
16 Individual photoelectrodes were used to measure  $V_{oc}$  against at most two redox couples, and were  
17 rinsed between testing with copious amounts of  $\text{CH}_3\text{CN}$ . Each photoelectrode was not used with  
18 more than two couples to avoid testing samples that may have degraded through use. This  
19 procedure guards against using samples in which Gr delaminated from the Si surface due to the  
20 capillary forces produced as the electrolyte solvent dries after cleaning or moving a single sample  
21 between different solutions. Because of this precaution, the values for  $V_{oc}$  have not been collected  
22 against the full range of redox couples for any single electrode. In contrast, due to the small spot  
23 size of SECCM, the full complement of redox couples were measured on a single  $1\text{ cm}^2$  sample  
24 that contained bare regions as well as regions covered separately by Gr and h-BN, thereby allowing  
25 their distinct behaviors to be elucidated.  
26  
27  
28  
29  
30  
31  
32  
33  
34  
35  
36  
37  
38  
39  
40  
41

42 Figure 3 shows the dependence of  $V_{oc}$  on the effective solution potential for macroscale p-Si-H,  
43 p-SiO<sub>x</sub>, p-Si/Gr, and p-Si/h-BN electrodes, respectively, in contact with  $\text{CH}_3\text{CN}$ -0.50 M  $\text{LiClO}_4$   
44 under  $100\text{ mW cm}^{-2}$  of ELH-type W-halogen simulated solar illumination. Each point represents  
45 an average of at least 5 electrodes, with standard deviations represented by the error bars. The  $V_{oc}$   
46 data for all redox couples are summarized in Table 1. In the macroscale measurements, the p-Si-  
47 H, p-SiO<sub>x</sub>, and p-Si/h-BN samples showed two distinct trends: regions at relatively positive or  
48 negative  $E_{\text{eff}}(\text{A}/\text{A}^-)$  in which  $V_{oc}$  was fixed with respect to  $E_{\text{eff}}(\text{A}/\text{A}^-)$ ; and a second region in which  
49  
50  
51  
52  
53  
54  
55  
56  
57  
58  
59  
60

$V_{oc}$  scaled approximately linearly with  $E_{eff}(A/A^-)$ . The slopes of  $V_{oc}$  with respect to  $E_{eff}(A/A^-)$  for p-Si-H surfaces were lower than those reported previously, but the maximum  $\Delta V_{oc}$  of  $505 \pm 53$  mV is comparable with the previously reported value of  $523 \pm 42$  mV.<sup>31</sup> The p-Si-H, p-SiO<sub>x</sub>, and p-Si/h-BN samples evaluated in this work displayed slopes,  $-\Delta V_{oc}/\Delta E_{eff}(A/A^-)$ , of  $\sim 0.41$ ,  $0.43$ , and  $0.45$ , respectively, while the p-Si/Gr samples had a lower slope of  $-\Delta V_{oc}/\Delta E_{eff}(A/A^-) \sim 0.24$  (Table S2). These electrodes also displayed the smallest change in  $V_{oc}$  across the full range of redox couples, with  $V_{oc}$  shifting only in contact with redox couples that had the most negative  $E_{eff}(A/A^-)$  values ( $E_{eff} \leq -0.35$  vs. SCE).

Figure 4 shows the dependence of  $V_{oc}$  on  $E_{eff}(A/A^-)$  for nanoscale p-SiO<sub>x</sub>, p-Si/Gr, and p-Si/h-BN electrodes, respectively, in contact with CH<sub>3</sub>CN–0.50 M LiClO<sub>4</sub> under 100 mW cm<sup>-2</sup> ELH-type illumination. The data for the nanoscale measurements displayed the same three regions observed in the macroscale  $V_{oc}$  measurements (Figure 3). The maximum  $\Delta V_{oc}$  for p-Si-H by SECCM was  $342 \pm 18$  mV, which is closer to  $401 \pm 33$  mV, the maximum  $\Delta V_{oc}$  value for the macroscale p-SiO<sub>x</sub> measurements than it is to the macroscale p-Si-H measurements. This behavior can be understood from the preparation of the SECCM sample. As the p-Si-H, p-Si/Gr, and p-Si/h-BN measurements were all taken on the same wafer chip, to ensure uniformity in sample preparation, the p-Si-H surface could not immediately be etched before testing by SECCM, leaving a small amount of oxide on the surface, similar to the preparation of the p-SiO<sub>x</sub> electrodes used in the macroscale electrode measurements. Table 1 summarizes the experimental conditions and all  $V_{oc}$  data for the macroscale and SECCM measurements.

## Discussion

1  
2  
3 The data shown above clearly demonstrate that in otherwise nominally identical interfaces, Gr  
4 shows markedly different behavior from h-BN. The higher density of states in Gr introduces  
5 surface states that decrease  $V_{oc}$  in both macroscale and nanoscale measurements. These data also  
6 indicate that the nanoscale and macroscale data show excellent congruency. Despite the extremely  
7 small contact area, nanoscale measurements consistently showed the same junction behavior as  
8 their macroscale counterparts. Solid-state point contacts can show ohmic behavior at otherwise  
9 rectifying junctions, so the ability to reliably produce nanoscale junctions that show the same  
10 behavior as their macroscale counterparts is significant. Although multiple effects may contribute  
11 to the quantitative differences between the measured quantities, the measurements are robust  
12 enough to reveal important differences between different interfaces and different scales.  
13  
14  
15  
16  
17  
18  
19  
20  
21  
22  
23  
24  
25

### 26 27 *Macroscale measurements*

28  
29  
30 The macroscale behavior of p-Si photoelectrodes can be divided into two groups: photoelectrodes  
31 with parallel slopes of  $\Delta V_{oc}/\Delta E_{eff}(A/A^-)$  (p-Si-H, p-SiO<sub>x</sub>, and p-Si/h-BN) and those without (p-  
32 Si/Gr). The differences in the values for  $V_{oc}$  between the macroscale p-Si/Gr and p-Si/h-BN  
33 samples can arise from the presence of oxide at the p-Si surface, increased surface recombination  
34 due to the surface oxide or defects in the polycrystalline 2D overlayer, and differences in the  
35 relative density of states of each polycrystalline 2D overlayer. Due to the nominally identical p-  
36 Si source and fabrication process, the effect of the oxide on  $V_{oc}$  can be quantified by directly  
37 comparing the p-Si-H and p-SiO<sub>x</sub> electrodes to show that  $V_{oc}$  was attenuated by  $\sim 0.1$  V in the  
38 presence of a thin oxide. XPS analysis showed that the p-SiO<sub>x</sub>, p-Si/Gr, and p-Si/h-BN electrodes  
39 all had similar amounts of oxide at the surface (Figure S1), hence this same decrease in  $V_{oc}$  is  
40 expected for the measurements at both the p-Si/Gr and p-Si/h-BN interfaces. However, this  
41 decrease in  $V_{oc}$  due to surface oxide does not fully account for the differences observed between  
42  
43  
44  
45  
46  
47  
48  
49  
50  
51  
52  
53  
54  
55  
56  
57  
58  
59  
60

1  
2  
3 the p-Si–H and p-Si/2D overlayer (p-Si/2D) photoelectrodes. The p-Si/h-BN interfaces showed an  
4 additional 65 mV decrease in  $V_{oc}$  compared to p-SiO<sub>x</sub>. The similarity in  $\Delta V_{oc}/\Delta E_{eff}(A/A^-)$  for the  
5 p-Si–H, p-SiO<sub>x</sub>, and p-Si/h-BN electrodes suggests that the change between p-SiO<sub>x</sub> and p-Si/h-BN  
6 should be treated as a linear decrease in the overall performance as compared to p-Si–H electrodes,  
7 analogous to the behavior when oxide is introduced onto a H-terminated p-Si electrode.<sup>32</sup> This h-  
8 BN overlayer is the primary difference between the p-SiO<sub>x</sub> and p-Si/hBN electrodes, which after  
9 annealing have mutually similar work functions and dipoles (Table S1). Thus, the additional 65  
10 mV loss in  $V_{oc}$  is attributable to the effects of the h-BN. Pristine h-BN does not have surface states  
11 within the band gap of Si, hence the small change in  $V_{oc}$  is likely the result of small increases in  
12 trap-state-mediated recombination ( $J_{br}$ ), and thus  $J_0$ , due to the polycrystalline nature of the h-BN  
13 used in this work. Polycrystalline, CVD-grown sheets of monolayer 2D material contribute to  
14 defects on the surface of a 2D material and provide sites for increased surface recombination.<sup>16, 33</sup>  
15 This behavior is consistent with expectations in which changes in the surface recombination  
16 velocity,  $S$ , affect  $V_{oc}$  but do not substantially affect the work function of a sample.<sup>34-35</sup> p-SiO<sub>x</sub>  
17 samples have a slightly lower  $S$  ( $= 3025 \text{ cm s}^{-1}$ ) than the p-Si/h-BN samples ( $S = 3905 \text{ cm s}^{-1}$ ).  
18 Similarly,  $J_0$  is higher by an order of magnitude for p-Si/h-BN in contact with Cp<sub>2</sub>Co<sup>+0</sup> than  $J_0$  for  
19 either p-Si–H or p-SiO<sub>x</sub>.  
20  
21  
22  
23  
24  
25  
26  
27  
28  
29  
30  
31  
32  
33  
34  
35  
36  
37  
38  
39  
40  
41  
42

43 Although the surface recombination velocity of p-Si/Gr (4064 cm s<sup>-1</sup>) is similar to that of p-Si/h-  
44 BN, and this interface has the same work function as p-SiO<sub>x</sub> and p-Si/h-BN, the p-Si/Gr electrodes  
45 display a lower value of  $\Delta V_{oc}/\Delta E_{eff}(A/A^-)$  over the same range of effective potentials, suggesting  
46 the predominance of a different mechanism to determine  $V_{oc}$  for these macroscale junctions. The  
47 fit chosen for the macroscale p-Si/Gr data is discussed in detail in the SI. The polycrystallinity of  
48 the Gr and h-BN used in this work could contribute to the smaller value for  $V_{oc}$  or range of tunable  
49  
50  
51  
52  
53  
54  
55  
56  
57  
58  
59  
60

1  
2  
3  $V_{oc}$  when compared to p-Si-H or p-SiO<sub>x</sub> electrodes, but cannot readily account for the differences  
4  
5 between the p-Si/Gr and p-Si/h-BN samples, because the grains of the h-BN used in this work  
6  
7 were an order of magnitude smaller than those in the Gr. If the crystallinity were the sole factor in  
8  
9 limiting the range of potentials at the interface, p-Si/h-BN would have lower values of  $V_{oc}$ , and  
10  
11 higher surface recombination velocities than p-Si/Gr samples, in contrast to the experimental  
12  
13 observations.  
14  
15

16  
17  
18 Measurements of the barrier height of n-Si/2D/metal Schottky diodes exhibit trends that are in  
19  
20 accord with the observations reported herein for semiconductor/liquid interfaces.<sup>6</sup> The decrease  
21  
22 in barrier height of both n-Si/2D/metal and p-Si/2D/liquid junctions suggests that limitations  
23  
24 imposed by device fabrication, rather than intrinsic polarization of the 2D overlayer, dominates  
25  
26 the formation of the interface dipole. Thus, the decrease in  $V_{oc}$  due to a surface dipole is more  
27  
28 consistently ascribed to increased surface recombination at the interface as opposed to the intrinsic  
29  
30 nature of the 2D material. The surface oxide, increase in recombination, and polycrystalline nature  
31  
32 of the 2D overlayer only partially account for the difference between p-Si-H and p-Si/Gr or p-  
33  
34 Si/h-BN, so the properties of the 2D material and interaction with the surface contribute  
35  
36 substantially to the observed differences in behavior of the semiconductor/liquid interfaces  
37  
38 investigated herein. The crystal structure and lattice constants for Gr and h-BN are nearly identical  
39  
40 and these 2D materials differ most prominently in their respective band gap (Figure S6). With a  
41  
42 limited density of states near its Fermi level, which is positioned mid-gap to silicon, the Gr in these  
43  
44 junctions exerts more influence on the interfacial energetics than h-BN, which has no states mid-  
45  
46 gap or near the conduction or valence band of Si. This characteristic leads to a more negative onset  
47  
48 in the slope of  $V_{oc}$  as well as a shallower slope of  $\Delta V_{oc}/\Delta E_{eff}(A/A^-)$ .  
49  
50  
51  
52  
53  
54  
55

### 56 *Nanoscale measurements*

57  
58  
59  
60

1  
2  
3 As shown in Figure 3 and 4, the fixed and sloping regions of  $V_{oc}$  with respect to solution potential  
4 measured by SECCM generally were in excellent agreement with their macroscale counterparts.  
5  
6 However, the values for  $V_{oc}$  of p-Si-H at the macroscale were consistently higher than those  
7  
8 observed by SECCM. The values of  $V_{oc}$  for p-Si-H by SECCM were much closer to the values of  
9  
10  $V_{oc}$  for the macroscale p-SiO<sub>x</sub> electrodes. This similarity follows from the XP spectra (Figure S1),  
11  
12 which shows that the same or a greater thickness of oxide was generated at the surface of the p-  
13  
14 SiO<sub>x</sub> electrodes as the p-Si/Gr and p-Si/h-BN electrodes during fabrication. Thus, the bare region  
15  
16 of the single electrode used for SECCM was more similar to the Si surface under Gr or h-BN than  
17  
18 to a freshly etched p-Si-H electrode. The presence of a surface oxide can thus consistently account  
19  
20 for a decrease in observed  $V_{oc}$  of ~ 100 mV for both p-Si/Gr and p-Si/h-BN electrodes.  
21  
22  
23  
24  
25

26  
27 Certain specific measurements, such as the  $V_{oc}$  of p-Si/h-BN in contact with Cp<sub>2</sub>Ni<sup>+0</sup>, were lower  
28  
29 for macroscale electrodes than were observed by SECCM. These differences were predominantly  
30  
31 observed for the less stable redox couples (i.e. Cp\*<sub>2</sub>Co<sup>+0</sup>, Cp<sub>2</sub>Ni<sup>+0</sup>). The slopes in  $V_{oc}$  for p-Si-H,  
32  
33 p-SiO<sub>x</sub> and p-Si/h-BN were identical, within experimental error, for the macroscale and SECCM  
34  
35 measurements, demonstrating that the observed trends were mutually consistent the same across  
36  
37 the macro and nanoscale.  
38  
39  
40

41  
42 The voltammetry (Figure 1-2) showed identical shapes between macroscale and SECCM  
43  
44 measurements but revealed different behavior between the different types of electrode. The p-Si-  
45  
46 H was strongly rectifying in contact with Cp<sub>2</sub>Co<sup>+0</sup> and had a high value of  $V_{oc}$  under illumination.  
47  
48 The p-Si/h-BN was also rectifying, but the shape of the  $J$ - $E$  characteristic under illumination  
49  
50 indicated much more resistive behavior than was observed for p-Si-H electrodes. Specifically, a  
51  
52 light-limited current was not reached until the potential was further negative than the window  
53  
54 shown. The p-Si/Gr interface was rectifying to Cp<sub>2</sub>Co<sup>+0</sup> and had a large dark saturation current  
55  
56  
57  
58  
59  
60

1  
2  
3 density ( $J_0 \sim -5 \text{ mA cm}^{-2}$ ) relative to the other interfaces ( $J_0 \sim -5 \times 10^{-3} \text{ mA cm}^{-2}$  for p-Si-H and p-  
4 SiO<sub>x</sub>;  $J_0 \sim -5 \times 10^{-2} \text{ mA cm}^{-2}$  for p-Si/h-BN). In contact with Cp<sub>2</sub>Fe<sup>+0</sup>, all samples were ohmic and  
5 displayed similar fill factors to the voltammetry in contact with Cp<sub>2</sub>Co<sup>+0</sup>. A spatial comparison  
6 of this behavior (Figure S9) demonstrated that the  $V_{oc}$  did not vary substantially across the surface  
7 in either sample, despite the presence of grain boundaries in the polycrystalline material. This  
8 uniformity, alongside the agreement between nanoscale and macroscale  $V_{oc}$  trends, provides  
9 support for the observation that grain boundaries in the 2D materials are not strongly contributing  
10 to the PEC behavior, as the SECCM measurements are made on a scale well below the size of  
11 individual grains of either Gr or h-BN. The ability of these liquid probes to replicate the ohmic or  
12 rectifying behavior of macroscale junctions is notable. Previous reports employing conductive  
13 AFM with Ni tips on n-Si/Gr showed ohmic behavior whereas macroscale n-Si/Gr/Ni junctions  
14 showed rectifying behavior.<sup>12</sup> Hence in contrast to metal probes, liquid probes provide more  
15 reliable information about nanoscale junction behavior and enhance the understanding of how  
16 nanoscale spatial heterogeneity of interstitial layers impacts macroscale junction behavior.  
17  
18  
19  
20  
21  
22  
23  
24  
25  
26  
27  
28  
29  
30  
31  
32  
33  
34  
35

36 Although the magnitude of  $V_{oc}$  measured using SECCM is not in precise agreement with that of  
37 macroscale measurements, several differences between these techniques could be responsible for  
38 the observed differences. Two cases in which the difference deviated from the observed trend are  
39 consistent with effects associated with the use of specific redox couples in the nanoscale junction  
40 (see SI). However, systemic differences were also observed. The most apparent difference in  
41 experimental conditions between the macroscale and SECCM measurements is the geometry of  
42 carrier transport due to the size of the liquid junction. In the macroscale case, the  
43 photoelectrochemical junctions are much larger than the depletion width ( $W$ ) of Si so carrier  
44 transport and band bending are one-dimensional. Because the radius of the liquid junction in our  
45  
46  
47  
48  
49  
50  
51  
52  
53  
54  
55  
56  
57  
58  
59  
60

1  
2  
3 SECCM measurements is typically smaller than  $W$  (between 100 and 185 nm for the couples used),  
4  
5 band bending will occur in a hemispherical volume of radius  $W$  centered around the liquid  
6  
7 nanojunction, as is seen using metal probes in SPM.<sup>36-37</sup> This geometry increases the number of  
8  
9 carriers that can be collected at the interface relative to the 1D case. In contrast, SECCM  
10  
11 measurements showed the same ohmic or rectifying behavior as the macroscale counterpart.  
12  
13

14  
15  
16 Despite this qualitative agreement in junction behavior, this transport geometry causes a secondary  
17  
18 effect that impacts the magnitude of  $V_{oc}$  measured at the nanoscale. For all rectifying junctions,  
19  
20 the  $V_{oc}$  measured by SECCM is lower than that observed by macroscale. This difference is  
21  
22 consistent with expectations for effects produced by hemispherical band bending occurring  
23  
24 entirely within a distance of  $W$  from the Si surface. Hemispherical band bending provides  
25  
26 substantially more opportunity for recombination than a 1D case, due to the increase in surface  
27  
28 area relative to volume. This increase in recombination decreases the collection efficiency of  
29  
30 photogenerated electrons relative to the more plentiful holes and ultimately would decrease the  
31  
32  $V_{oc}$ .<sup>38</sup> As they are similarly affected, the drop in  $V_{oc}$  is nearly identical for p-SiO<sub>x</sub> and p-Si/h-BN.  
33  
34  
35 While p-Si/Gr electrodes are affected by this process, they also show nonzero values for  $V_{oc}$  of  
36  
37 0.021±0.004 V by SECCM in the lower plateau in which junctions exhibit ohmic behavior, as  
38  
39 opposed to the 0.006±0.007 V observed in macroscale measurements. This nonzero plateau could  
40  
41 arise from the combination of overfill illumination and the high conductivity of Gr enabling lateral  
42  
43 conduction of carriers from a significantly larger region of the sample than expected from the size  
44  
45 of the liquid junction. Transfer of photogenerated electrons from the Si to the Gr would compete  
46  
47 with recombination and enhance the photocurrent at the liquid junction, thus increasing the  
48  
49 measured  $V_{oc}$ . Both of the above cases represent fundamental limitations of nanoscale junctions  
50  
51 on macroscale photoelectrodes. Future studies utilizing finite element modeling could potentially  
52  
53  
54  
55  
56  
57  
58  
59  
60



1  
2  
3 deconvolute these effects from other differences at the surface, as has been done previously  
4  
5 to improve understanding of carrier transport in other scanning probe microscopies.<sup>39-40</sup> Despite  
6  
7 the present limits of this technique, the agreement between trends in  $V_{oc}$  vs.  $E_{eff}$  for macroscale and  
8  
9 SECCM measurements shows that despite the difference in carrier transport the same trend is  
10  
11 observed between nanoscale and macroscale contacts.  
12  
13

## 14 15 **Conclusions**

16  
17  
18 Compared to H-terminated p-Si electrodes using the same electrolyte, the  $V_{oc}$  values of p-Si  
19  
20 electrodes coated with highly conductive or insulating 2D materials, graphene ( $E_g$  0 eV) and  
21  
22 hexagonal boron nitride ( $E_g$  5.97 eV) respectively, demonstrate that the properties of these  
23  
24 interfaces are dependent primarily on the position of the Fermi level and density of states of the  
25  
26 2D material relative to band edges of the chosen semiconductor. Both Gr and h-BN-coated p-Si  
27  
28 photoelectrodes displayed lower open circuit-voltages in contact with a series of redox couples in  
29  
30 solution than bare p-Si-H photoelectrodes. Gr coated p-Si electrodes have a high density of states  
31  
32 at the 2D material, causing some Fermi level pinning. Despite the high density of states of  
33  
34 graphene, the pinning is moderate because only a single layer of atoms is required for full surface  
35  
36 coverage, ultimately minimizing the density of states introduced at the surface. Hence even highly  
37  
38 conductive 2D materials can be useful as protecting layers with minimal effects due to Fermi level  
39  
40 pinning. For h-BN coated p-Si electrodes, the 2D material has a low density of states, and thereby  
41  
42 avoids pinning due to introduced surface states. However, the oxide formed during transfer of  
43  
44 either 2D material and subsequent processing of the electrode interacts with the electrical character  
45  
46 of the 2D material to introduce surface dipoles that shifts the band positions of the semiconductor  
47  
48 surface to more negative values. These results indicate that exploration of 2D materials with  
49  
50 greater differences in electronegativity, in conjunction with transfer methods that prevent oxide  
51  
52  
53  
54  
55  
56  
57  
58  
59  
60

1  
2  
3 formation, could allow facile tuning of band energetics through the use of 2D materials as  
4  
5 protecting layers for semiconductors.  
6  
7

8  
9 SECCM can thus provide a useful technique for evaluation of the  $V_{oc}$  of 2D semiconductor  
10 photoelectrodes. These results provide a definitive demonstration of  $V_{oc}$  measurements by  
11 SECCM, in conjunction with a unique ability among microscopy techniques to assess the utility  
12  
13 of nanoscale heterojunctions to replicate the ohmic or rectifying behavior of macroscale  
14  
15 measurements using nominally identical electrodes and electrolyte solutions in each case. This  
16  
17 feature makes, for the first time, reliable measurements of nanoscale photoelectrochemistry viable,  
18  
19 and provides a path to studying materials with nanoscale heterogeneity that impacts macroscale  
20  
21 performance. Additionally, nanoscale SECCM measurements of  $V_{oc}$  replicate trends observed at  
22  
23 the macroscale, though quantitative differences are evident in the case of Gr. Moreover, SECCM  
24  
25 allowed measurement of the variation in  $V_{oc}$  between coated and uncoated regions of a 2D material  
26  
27 on a single p-Si electrode, demonstrating applicability for imaging semiconductor/liquid junction  
28  
29 energetics with nanoscale resolution.  
30  
31  
32  
33  
34  
35  
36  
37  
38  
39  
40  
41  
42  
43  
44  
45  
46  
47  
48  
49  
50  
51  
52  
53  
54  
55  
56  
57  
58  
59  
60

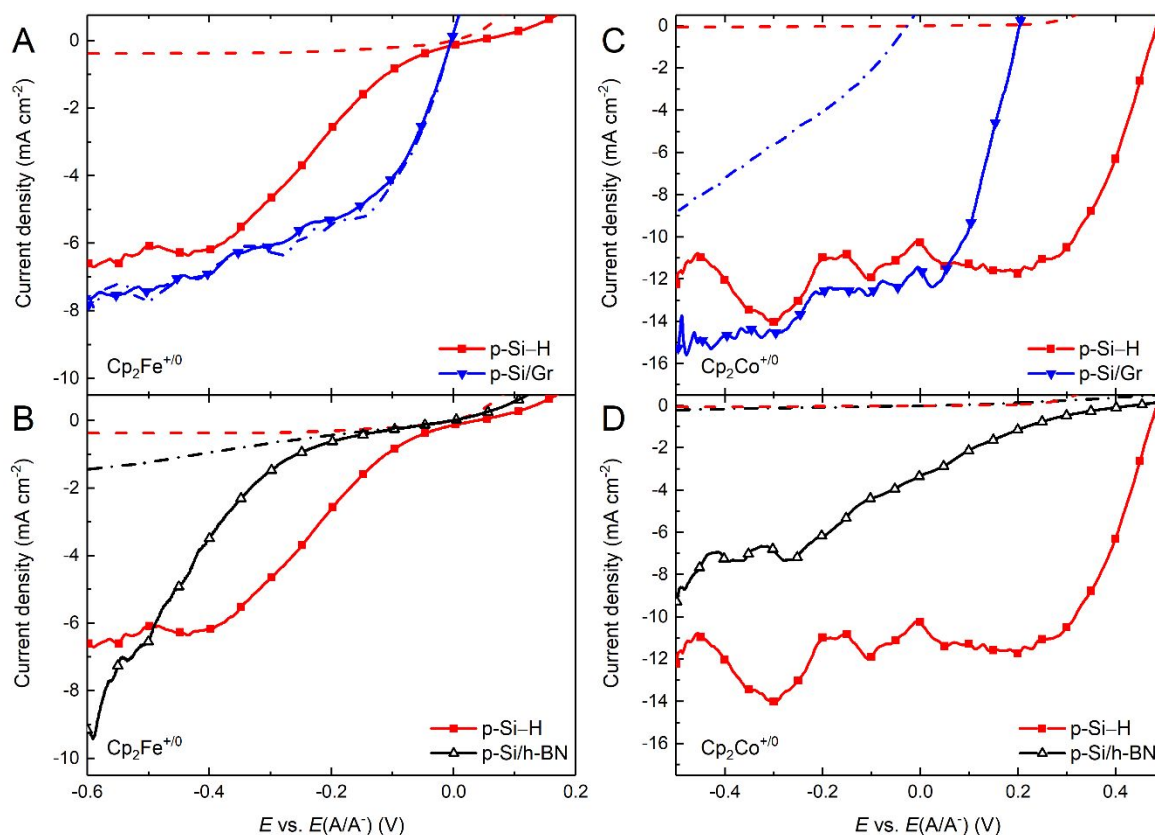


**Figure 1.** Current density vs potential ( $J$ - $E$ ) behavior of modified p-Si electrodes in contact with  $\text{Cp}_2\text{Fe}^{+/0}$  (A-B) and  $\text{Cp}_2\text{Co}^{+/0}$  (C-D), in  $\text{CH}_3\text{CN}$ -0.50 M  $\text{LiClO}_4$  under  $100 \text{ mW cm}^{-2}$  of ELH-type simulated solar illumination. The dashed lines show scans of the same electrodes without illumination. In contact with either redox couple, the fill factor of the p-Si/h-BN electrode was substantially smaller than that of either the p-Si-H (Figure 1) or p-SiO<sub>x</sub> (Figure S7) electrodes, indicative of slow electron-transfer kinetics at the h-BN/liquid interface. In contact with  $\text{Cp}_2\text{Co}^{+/0}$ , the  $J$ - $E$  characteristics of the p-Si/Gr electrode shifted upon illumination, in addition to displaying substantially larger reverse saturation current densities than the other three types of electrodes.

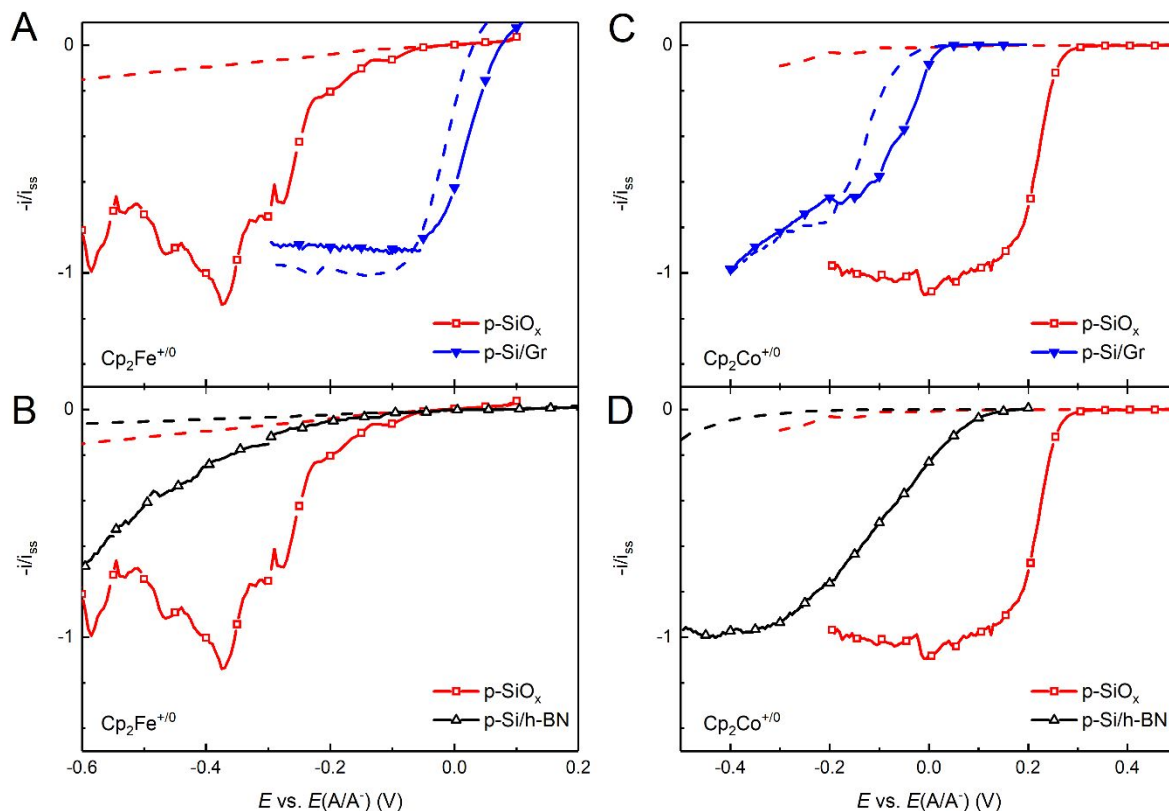


**Figure 2.** Current vs potential ( $I-E$ ) behavior in contact with  $CH_3CN-0.50$  M  $LiClO_4$  under  $100$   $mW\ cm^{-2}$  of ELH-type simulated solar illumination determined by SECCM for p-Si electrodes in contact with  $Cp_2Fe^{+/0}$  (A-B) and  $Cp_2Co^{+/0}$  (C-D). The dashed lines show scans of the same electrodes without illumination. The data in SECCM measurements were similar to data observed in the macroscale measurements (Figure 1). Si-H surfaces were not probed by SECCM because the  $O_2$  and water content in the flush box used for these experiments resulted in the formation of oxide on freshly etched Si-H samples more rapidly than measurements could be performed.

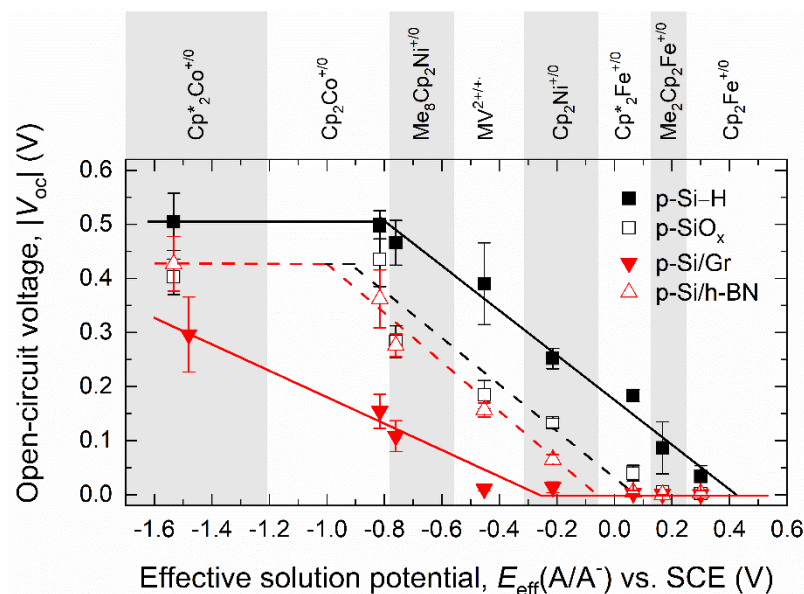
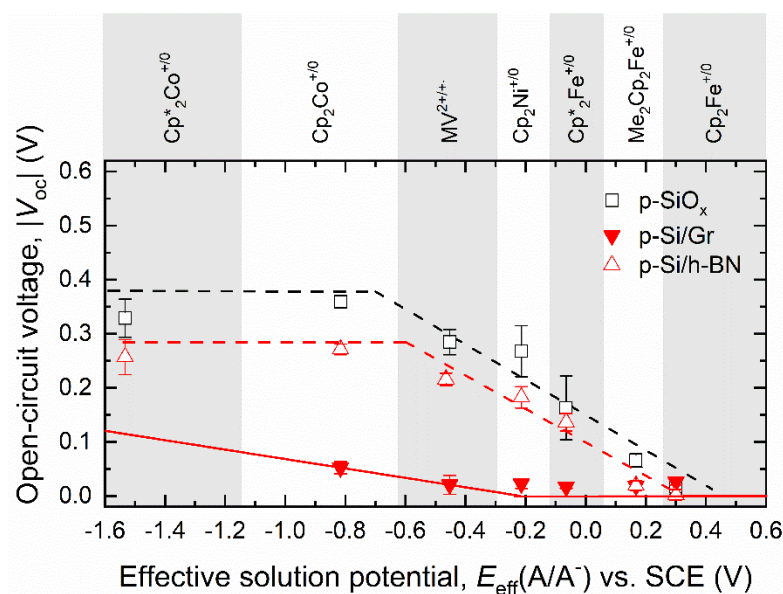


**Figure 3.** Comparison of open-circuit voltage of macroscale p-Si-H, p-SiO<sub>x</sub>, p-Si/Gr, and p-Si/h-BN electrodes, respectively, versus the effective redox potential of various redox couples. Three regions, each highlighted by linear fits of the data therein, were identified for all samples.



1  
2  
3 **Figure 4.** Comparison of the open-circuit voltage of p-SiO<sub>x</sub>, p-Si/Gr, and p-Si/h-BN electrodes,  
4 respectively, versus the effective potential of various redox couples, on the same SECCM  
5 electrode. Linear fits of the data have been used to highlight the different regions of behavior.  
6  
7  
8  
9  
10  
11  
12  
13  
14  
15  
16  
17  
18  
19  
20  
21  
22  
23  
24  
25  
26  
27  
28  
29  
30  
31  
32  
33  
34  
35  
36  
37  
38  
39  
40  
41  
42  
43  
44  
45  
46  
47  
48  
49  
50  
51  
52  
53  
54  
55  
56  
57  
58  
59  
60

Table 1. Summary of experimentally measured  $V_{oc}$ <sup>a</sup>

Redox couple <sup>a</sup>	effective potential vs. SCE <sup>b</sup> (V)	$V_{oc}$ (V) from macroscale electrodes				$V_{oc}$ (V) from SECCM electrode		
		p-Si-H	p-SiO <sub>x</sub>	p-Si/Gr	p-Si/h-BN	p-Si-H	p-Si/Gr	p-Si/h-BN
Cp* <sub>2</sub> Co <sup>+0</sup>	-0.963	0.505(53)	0.403(33)	0.296(70) <sup>c</sup>	0.427(50)	0.329(35)	- <sup>d</sup>	0.257(32)
Cp <sub>2</sub> Co <sup>+0</sup>	-0.816	0.499(26)	0.436(50)	0.154(32) <sup>c</sup>	0.362(54) <sup>c</sup>	0.360(11)	0.052(11)	0.272(10)
Me <sub>8</sub> Cp <sub>2</sub> Ni <sup>+0</sup>	-0.760	0.466(41)	0.283(29)	0.108(28)	0.276(21)	-	-	-
MV <sup>2+/+</sup>	-0.453	0.390(76)	0.185(26)	0.011(3)	0.157(13)	0.285(23)	0.021(18)	0.216(11)
Cp <sub>2</sub> Ni <sup>+0</sup>	-0.214	0.252(19)	0.133(9)	0.014(10) <sup>c</sup>	0.065(9) <sup>c</sup>	0.268(47)	0.023(9)	0.183(20)
Cp* <sub>2</sub> Fe <sup>+0</sup>	0.065	0.183(11)	0.040(14)	0.003(1)	0.005(3)	0.163(60)	0.017(3)	0.136(16)
Me <sub>2</sub> Cp <sub>2</sub> Fe <sup>+0</sup>	0.167	0.087(48)	0.005(3)	0	0	0.066(12)	0.018(5)	0.019(9)
Cp <sub>2</sub> Fe <sup>+0</sup>	0.171	0.034(20)	0.002(1)	0	0.003(5)	0.018(14)	0.026(5)	0.002(10)

<sup>a</sup> Each value of  $V_{oc}$  represents measurements from at least six photoelectrodes on the macroscale and at least three spots by SECCM. Standard deviations are given in parentheses, where appropriate, and are in units of mV. Abbreviations for the couples used are given in the Methods section.

<sup>b</sup> The effective cell potential was calculated using the equation  $E_{eff}(A/A^-) = E(A/A^-) - \frac{k_B T}{q} \ln \frac{[A_{eff}]}{[A]}$ , where  $E(A/A^-)$  was the cell potential of the redox couple vs. SCE,  $[A]$  was the minority acceptor concentration, and  $[A_{eff}] = 10$  mM. These values are reported vs SCE, which taken to be +0.197 V vs. NHE in this work.

<sup>c</sup> In select instances for macroscale testing, new solutions with slightly different potentials than those listed here were made to retest certain electrodes. The potentials of these solutions are not tabulated here but are shown correctly in Figure 3.

<sup>d</sup> Due to the lack of stability in the Cp\*<sub>2</sub>Co<sup>+0</sup> couple, no SECCM measurements could be collected for the p-Si/Gr interface

## ASSOCIATED CONTENT

**Supporting Information.**

The Supporting Information is available free of charge on the ACS Publications website at DOI:  
10.1021/acsnano.XXXXXXX.

- Figures S1-S6 and Table S1 contain XPS, UPS, Raman maps, UV-Vis spectra, and Tauc plots characterizing the 2D materials and 2d material coated p-Si
- Figure S7 contains data for cyclic voltammetry of p-SiO<sub>x</sub> electrodes
- Figure S8 and Table S2 contain alternate linear fits and their parameters for V<sub>oc</sub> measurements on macroscale p-Si/Gr electrodes
- Figure S9 contains V<sub>oc</sub> data taken in line scans using SECCM
- S1 discusses the calculation of effective solution potentials and Table S3 contains experimental redox couple concentrations, the standard reduction potential, and the effective solution potential calculated from these numbers
- S2 discusses redox couple compatibility with nanoscale junctions

nnXXXXXXXX.pdf (PDF)

## AUTHOR INFORMATION

**Corresponding Author**

\*E-mail: nslewis@caltech.edu



## Author Contributions

The manuscript was written through contributions of all authors. All authors have given approval to the final version of the manuscript. ‡These authors contributed equally. (match statement to author names with a symbol)

## Notes

The authors declare no competing financial interests.

## ACKNOWLEDGMENT

This work was supported by the Department of Energy, Basic Energy Sciences, grant DE-FG02-03ER15483. ACT acknowledges the National Science Foundation for a graduate fellowship. SECCM, UV-Vis, and XPS data were collected at the Molecular Materials Research Center in the Beckman Institute of the California Institute of Technology. We gratefully acknowledge the critical support and infrastructure provided for this work by The Kavli Nanoscience Institute at Caltech.

## REFERENCES

(1) Nielander, A. C.; Bierman, M. J.; Petrone, N.; Strandwitz, N. C.; Ardo, S.; Yang, F.; Hone, J.; Lewis, N. S., Photoelectrochemical Behavior of N-Type Si(111) Electrodes Coated with a Single Layer of Graphene. *J. Am. Chem. Soc.* **2013**, *135*, 17246-17249.

(2) Nielander, A. C.; Thompson, A. C.; Roske, C. W.; Maslyn, J. A.; Hao, Y.; Plymale, N. T.; Hone, J.; Lewis, N. S., Lightly Fluorinated Graphene As a Protective Layer for N-Type Si(111) Photoanodes in Aqueous Electrolytes. *Nano Lett.* **2016**, *16*, 4082-4086.

1  
2  
3 (3) Takahashi, T.; Tokailin, H.; Sagawa, T., Angle-Resolved Ultraviolet Photoelectron  
4 Spectroscopy of the Unoccupied Band Structure of Graphite. *Phys. Rev. B* **1985**, *32*, 8317-8324.

5  
6  
7  
8 (4) Novoselov, K. S.; Geim, A. K.; Morozov, S. V.; Jiang, D.; Zhang, Y.; Dubonos, S. V.;  
9 Grigorieva, I. V.; Firsov, A. A., Electric Field Effect in Atomically Thin Carbon Films. *Science*  
10 **2004**, *306*, 666-669.

11  
12  
13 (5) Di Bartolomeo, A., Graphene Schottky Diodes: An Experimental Review of the Rectifying  
14 Graphene/Semiconductor Heterojunction. *Phys. Rep.* **2016**, *606*, 1-58.

15  
16  
17 (6) Lee, M.-H.; Cho, Y.; Byun, K.-E.; Shin, K. W.; Nam, S.-G.; Kim, C.; Kim, H.; Han, S.-A.;  
18 Kim, S.-W.; Shin, H.-J.; Park, S., Two-Dimensional Materials Inserted at the  
19 Metal/Semiconductor Interface: Attractive Candidates for Semiconductor Device Contacts. *Nano*  
20 *Lett.* **2018**, *18*, 4878-4884.

21  
22 (7) Yoon, H. H.; Jung, S.; Choi, G.; Kim, J.; Jeon, Y.; Kim, Y. S.; Jeong, H. Y.; Kim, K.; Kwon,  
23 S.-Y.; Park, K., Strong Fermi-Level Pinning at Metal/N-Si(001) Interface Ensured by Forming an  
24 Intact Schottky Contact with a Graphene Insertion Layer. *Nano Lett.* **2017**, *17*, 44-49.

25  
26 (8) Cassabois, G.; Valvin, P.; Gil, B., Hexagonal Boron Nitride Is an Indirect Bandgap  
27 Semiconductor. *Nat. Photonics* **2016**, *10*, 262-266.

28  
29 (9) Chen, D.; Zhang, H.; Liu, Y.; Li, J., Graphene and Its Derivatives for the Development of  
30 Solar Cells, Photoelectrochemical, and Photocatalytic Applications. *Energ. Environ. Sci.* **2013**, *6*,  
31 1362-1387.

32  
33 (10) Britnell, L.; Gorbachev, R. V.; Jalil, R.; Belle, B. D.; Schedin, F.; Katsnelson, M. I.; Eaves,  
34 L.; Morozov, S. V.; Mayorov, A. S.; Peres, N. M. R.; Castro Neto, A. H.; Leist, J.; Geim, A. K.;

1  
2  
3 Ponomarenko, L. A.; Novoselov, K. S., Electron Tunneling through Ultrathin Boron Nitride  
4 Crystalline Barriers. *Nano Lett.* **2012**, *12*, 1707-1710.

7  
8 (11) Meng, J.-H.; Liu, X.; Zhang, X.-W.; Zhang, Y.; Wang, H.-L.; Yin, Z.-G.; Zhang, Y.-Z.;  
9 Liu, H.; You, J.-B.; Yan, H., Interface Engineering for Highly Efficient Graphene-on-Silicon  
10 Schottky Junction Solar Cells by Introducing a Hexagonal Boron Nitride Interlayer. *Nano Energy*  
11 **2016**, *28*, 44-50.

12  
13 (12) Byun, K.-E.; Chung, H.-J.; Lee, J.; Yang, H.; Song, H. J.; Heo, J.; Seo, D. H.; Park, S.;  
14 Hwang, S. W.; Yoo, I.; Kim, K., Graphene for True Ohmic Contact at Metal–Semiconductor  
15 Junctions. *Nano Lett.* **2013**, *13*, 4001-4005.

16  
17 (13) Khomyakov, P. A.; Giovannetti, G.; Rusu, P. C.; Brocks, G.; van den Brink, J.; Kelly, P. J.,  
18 First-Principles Study of the Interaction and Charge Transfer between Graphene and Metals. *Phys.*  
19 *Rev. B* **2009**, *79*, 195425.

20  
21 (14) Bokdam, M.; Brocks, G.; Katsnelson, M. I.; Kelly, P. J., Schottky Barriers at Hexagonal  
22 Boron Nitride/Metal Interfaces: A First-Principles Study. *Phys. Rev. B* **2014**, *90*, 085415.

23  
24 (15) Leong, W. S.; Luo, X.; Li, Y.; Khoo, K. H.; Quek, S. Y.; Thong, J. T. L., Low Resistance  
25 Metal Contacts to MoS<sub>2</sub> Devices with Nickel-Etched-Graphene Electrodes. *ACS Nano* **2015**, *9*,  
26 869-877.

27  
28 (16) Denis, P. A.; Iribarne, F., Comparative Study of Defect Reactivity in Graphene. *J. Phys.*  
29 *Chem. C* **2013**, *117*, 19048-19055.

1  
2  
3 (17) Ebejer, N.; Schnippering, M.; Colburn, A. W.; Edwards, M. A.; Unwin, P. R., Localized  
4 High Resolution Electrochemistry and Multifunctional Imaging: Scanning Electrochemical Cell  
5  
6  
7  
8 Microscopy. *Anal. Chem.* **2010**, *82*, 9141-9145.  
9

10  
11 (18) Snowden, M. E.; Güell, A. G.; Lai, S. C. S.; McKelvey, K.; Ebejer, N.; O'Connell, M. A.;  
12 Colburn, A. W.; Unwin, P. R., Scanning Electrochemical Cell Microscopy: Theory and  
13  
14  
15 Experiment for Quantitative High Resolution Spatially-Resolved Voltammetry and Simultaneous  
16  
17  
18 Ion-Conductance Measurements. *Anal. Chem.* **2012**, *84*, 2483-2491.  
19

20  
21 (19) Güell, A. G.; Cuharuc, A. S.; Kim, Y.-R.; Zhang, G.; Tan, S.-y.; Ebejer, N.; Unwin, P. R.,  
22  
23  
24 Redox-Dependent Spatially Resolved Electrochemistry at Graphene and Graphite Step Edges.  
25  
26  
27 *ACS Nano* **2015**, *9*, 3558-3571.  
28

29  
30 (20) Aaronson, B. D. B.; Byers, J. C.; Colburn, A. W.; McKelvey, K.; Unwin, P. R., Scanning  
31  
32  
33 Electrochemical Cell Microscopy Platform for Ultrasensitive Photoelectrochemical Imaging.  
34  
35  
36 *Anal. Chem.* **2015**, *87*, 4129-4133.  
37

38  
39 (21) Chen, R.; Nioradze, N.; Santhosh, P.; Li, Z.; Surwade, S. P.; Shenoy, G. J.; Parobek, D. G.;  
40  
41  
42 Kim, M. A.; Liu, H.; Amemiya, S., Ultrafast Electron Transfer Kinetics of Graphene Grown by  
43  
44  
45 Chemical Vapor Deposition. *Angew. Chem. Int. Ed.* **2015**, *54*, 15134-15137.  
46

47  
48 (22) Tan, C.; Rodríguez-López, J.; Parks, J. J.; Ritzert, N. L.; Ralph, D. C.; Abruña, H. D.,  
49  
50  
51  
52  
53  
54  
55  
56  
57  
58  
59  
60  
61  
62  
63  
64  
65  
66  
67  
68  
69  
70  
71  
72  
73  
74  
75  
76  
77  
78  
79  
80  
81  
82  
83  
84  
85  
86  
87  
88  
89  
90  
91  
92  
93  
94  
95  
96  
97  
98  
99  
100  
101  
102  
103  
104  
105  
106  
107  
108  
109  
110  
111  
112  
113  
114  
115  
116  
117  
118  
119  
120  
121  
122  
123  
124  
125  
126  
127  
128  
129  
130  
131  
132  
133  
134  
135  
136  
137  
138  
139  
140  
141  
142  
143  
144  
145  
146  
147  
148  
149  
150  
151  
152  
153  
154  
155  
156  
157  
158  
159  
160  
161  
162  
163  
164  
165  
166  
167  
168  
169  
170  
171  
172  
173  
174  
175  
176  
177  
178  
179  
180  
181  
182  
183  
184  
185  
186  
187  
188  
189  
190  
191  
192  
193  
194  
195  
196  
197  
198  
199  
200  
201  
202  
203  
204  
205  
206  
207  
208  
209  
210  
211  
212  
213  
214  
215  
216  
217  
218  
219  
220  
221  
222  
223  
224  
225  
226  
227  
228  
229  
230  
231  
232  
233  
234  
235  
236  
237  
238  
239  
240  
241  
242  
243  
244  
245  
246  
247  
248  
249  
250  
251  
252  
253  
254  
255  
256  
257  
258  
259  
260  
261  
262  
263  
264  
265  
266  
267  
268  
269  
270  
271  
272  
273  
274  
275  
276  
277  
278  
279  
280  
281  
282  
283  
284  
285  
286  
287  
288  
289  
290  
291  
292  
293  
294  
295  
296  
297  
298  
299  
300  
301  
302  
303  
304  
305  
306  
307  
308  
309  
310  
311  
312  
313  
314  
315  
316  
317  
318  
319  
320  
321  
322  
323  
324  
325  
326  
327  
328  
329  
330  
331  
332  
333  
334  
335  
336  
337  
338  
339  
340  
341  
342  
343  
344  
345  
346  
347  
348  
349  
350  
351  
352  
353  
354  
355  
356  
357  
358  
359  
360  
361  
362  
363  
364  
365  
366  
367  
368  
369  
370  
371  
372  
373  
374  
375  
376  
377  
378  
379  
380  
381  
382  
383  
384  
385  
386  
387  
388  
389  
390  
391  
392  
393  
394  
395  
396  
397  
398  
399  
400  
401  
402  
403  
404  
405  
406  
407  
408  
409  
410  
411  
412  
413  
414  
415  
416  
417  
418  
419  
420  
421  
422  
423  
424  
425  
426  
427  
428  
429  
430  
431  
432  
433  
434  
435  
436  
437  
438  
439  
440  
441  
442  
443  
444  
445  
446  
447  
448  
449  
450  
451  
452  
453  
454  
455  
456  
457  
458  
459  
460  
461  
462  
463  
464  
465  
466  
467  
468  
469  
470  
471  
472  
473  
474  
475  
476  
477  
478  
479  
480  
481  
482  
483  
484  
485  
486  
487  
488  
489  
490  
491  
492  
493  
494  
495  
496  
497  
498  
499  
500  
501  
502  
503  
504  
505  
506  
507  
508  
509  
510  
511  
512  
513  
514  
515  
516  
517  
518  
519  
520  
521  
522  
523  
524  
525  
526  
527  
528  
529  
530  
531  
532  
533  
534  
535  
536  
537  
538  
539  
540  
541  
542  
543  
544  
545  
546  
547  
548  
549  
550  
551  
552  
553  
554  
555  
556  
557  
558  
559  
560  
561  
562  
563  
564  
565  
566  
567  
568  
569  
570  
571  
572  
573  
574  
575  
576  
577  
578  
579  
580  
581  
582  
583  
584  
585  
586  
587  
588  
589  
590  
591  
592  
593  
594  
595  
596  
597  
598  
599  
600  
601  
602  
603  
604  
605  
606  
607  
608  
609  
610  
611  
612  
613  
614  
615  
616  
617  
618  
619  
620  
621  
622  
623  
624  
625  
626  
627  
628  
629  
630  
631  
632  
633  
634  
635  
636  
637  
638  
639  
640  
641  
642  
643  
644  
645  
646  
647  
648  
649  
650  
651  
652  
653  
654  
655  
656  
657  
658  
659  
660  
661  
662  
663  
664  
665  
666  
667  
668  
669  
670  
671  
672  
673  
674  
675  
676  
677  
678  
679  
680  
681  
682  
683  
684  
685  
686  
687  
688  
689  
690  
691  
692  
693  
694  
695  
696  
697  
698  
699  
700  
701  
702  
703  
704  
705  
706  
707  
708  
709  
710  
711  
712  
713  
714  
715  
716  
717  
718  
719  
720  
721  
722  
723  
724  
725  
726  
727  
728  
729  
730  
731  
732  
733  
734  
735  
736  
737  
738  
739  
740  
741  
742  
743  
744  
745  
746  
747  
748  
749  
750  
751  
752  
753  
754  
755  
756  
757  
758  
759  
760  
761  
762  
763  
764  
765  
766  
767  
768  
769  
770  
771  
772  
773  
774  
775  
776  
777  
778  
779  
780  
781  
782  
783  
784  
785  
786  
787  
788  
789  
790  
791  
792  
793  
794  
795  
796  
797  
798  
799  
800  
801  
802  
803  
804  
805  
806  
807  
808  
809  
810  
811  
812  
813  
814  
815  
816  
817  
818  
819  
820  
821  
822  
823  
824  
825  
826  
827  
828  
829  
830  
831  
832  
833  
834  
835  
836  
837  
838  
839  
840  
841  
842  
843  
844  
845  
846  
847  
848  
849  
850  
851  
852  
853  
854  
855  
856  
857  
858  
859  
860  
861  
862  
863  
864  
865  
866  
867  
868  
869  
870  
871  
872  
873  
874  
875  
876  
877  
878  
879  
880  
881  
882  
883  
884  
885  
886  
887  
888  
889  
890  
891  
892  
893  
894  
895  
896  
897  
898  
899  
900  
901  
902  
903  
904  
905  
906  
907  
908  
909  
910  
911  
912  
913  
914  
915  
916  
917  
918  
919  
920  
921  
922  
923  
924  
925  
926  
927  
928  
929  
930  
931  
932  
933  
934  
935  
936  
937  
938  
939  
940  
941  
942  
943  
944  
945  
946  
947  
948  
949  
950  
951  
952  
953  
954  
955  
956  
957  
958  
959  
960  
961  
962  
963  
964  
965  
966  
967  
968  
969  
970  
971  
972  
973  
974  
975  
976  
977  
978  
979  
980  
981  
982  
983  
984  
985  
986  
987  
988  
989  
990  
991  
992  
993  
994  
995  
996  
997  
998  
999  
1000

1  
2  
3 (23) Todt, M. A.; Isenberg, A. E.; Nanayakkara, S. U.; Miller, E. M.; Sambur, J. B., Single-  
4 Nanoflake Photo-Electrochemistry Reveals Champion and Spectator Flakes in Exfoliated MoSe<sub>2</sub>  
5 Films. *J. Phys. Chem. C* **2018**, *122*, 6539-6545.  
6  
7

8  
9  
10 (24) Ghilane, J.; Hapiot, P.; Bard, A. J., Metal/Polypyrrole Quasi-Reference Electrode for  
11 Voltammetry in Nonaqueous and Aqueous Solutions. *Anal. Chem.* **2006**, *78*, 6868-6872.  
12  
13

14  
15 (25) Kim, J.; Shen, M.; Nioradze, N.; Amemiya, S., Stabilizing Nanometer Scale Tip-to-  
16 Substrate Gaps in Scanning Electrochemical Microscopy Using an Isothermal Chamber for  
17 Thermal Drift Suppression. *Anal. Chem.* **2012**, *84*, 3489-3492.  
18  
19  
20

21 (26) Li, X.; Zhu, Y.; Cai, W.; Borysiak, M.; Han, B.; Chen, D.; Piner, R. D.; Colombo, L.; Ruoff,  
22 R. S., Transfer of Large-Area Graphene Films for High-Performance Transparent Conductive  
23 Electrodes. *Nano Lett.* **2009**, *9*, 4359-4363.  
24  
25  
26

27 (27) Pirkle, A.; Chan, J.; Venugopal, A.; Hinojos, D.; Magnuson, C. W.; McDonnell, S.;  
28 Colombo, L.; Vogel, E. M.; Ruoff, R. S.; Wallace, R. M., The Effect of Chemical Residues on the  
29 Physical and Electrical Properties of Chemical Vapor Deposited Graphene Transferred to SiO<sub>2</sub>.  
30 *Appl. Phys. Lett.* **2011**, *99*, 122108.  
31  
32  
33

34 (28) Suk, J. W.; Kitt, A.; Magnuson, C. W.; Hao, Y.; Ahmed, S.; An, J.; Swan, A. K.; Goldberg,  
35 B. B.; Ruoff, R. S., Transfer of CVD-grown Monolayer Graphene onto Arbitrary Substrates. *ACS*  
36 *Nano* **2011**, *5*, 6916-6924.  
37  
38  
39

40 (29) Bentley, C. L.; Kang, M.; Unwin, P. R., Nanoscale Structure Dynamics within  
41 Electrocatalytic Materials. *J. Am. Chem. Soc.* **2017**, *139*, 16813-16821.  
42  
43  
44  
45  
46  
47  
48  
49  
50  
51  
52  
53  
54  
55  
56  
57  
58  
59  
60

1  
2  
3 (30) Bentley, C. L.; Kang, M.; Maddar, F. M.; Li, F.; Walker, M.; Zhang, J.; Unwin, P. R.,  
4  
5 Electrochemical Maps and Movies of the Hydrogen Evolution Reaction on Natural Crystals of  
6  
7 Molybdenite (MoS<sub>2</sub>): Basal Vs. Edge Plane Activity. *Chem. Sci.* **2017**, *8*, 6583-6593.

8  
9  
10 (31) Grimm, R. L.; Bierman, M. J.; O'Leary, L. E.; Strandwitz, N. C.; Brunshwig, B. S.; Lewis,  
11  
12 N. S., Comparison of the Photoelectrochemical Behavior of H-Terminated and Methyl-terminated  
13  
14 Si(111) Surfaces in Contact with a Series of One-Electron, Outer-Sphere Redox Couples in  
15  
16 CH<sub>3</sub>CN. *J. Phys. Chem. C* **2012**, *116*, 23569-23576.

17  
18  
19 (32) Lewis, N. S., A Quantitative Investigation of the Open-Circuit Photovoltage at the  
20  
21 Semiconductor/Liquid Interface. *J. Electrochem. Soc.* **1984**, *131*, 2496-2503.

22  
23 (33) Banhart, F.; Kotakoski, J.; Krasheninnikov, A. V., Structural Defects in Graphene. *ACS*  
24  
25 *Nano* **2011**, *5*, 26-41.

26  
27 (34) Serpone, N.; Pelizzetti, E., *Photocatalysis : Fundamentals and Applications*. Wiley: New  
28  
29 York, 1989.

30  
31 (35) Gleason-Rohrer, D. C.; Brunshwig, B. S.; Lewis, N. S., Measurement of the Band Bending  
32  
33 and Surface Dipole at Chemically Functionalized Si(111)/Vacuum Interfaces. *J. Phys. Chem. C*  
34  
35 **2013**, *117*, 18031-18042.

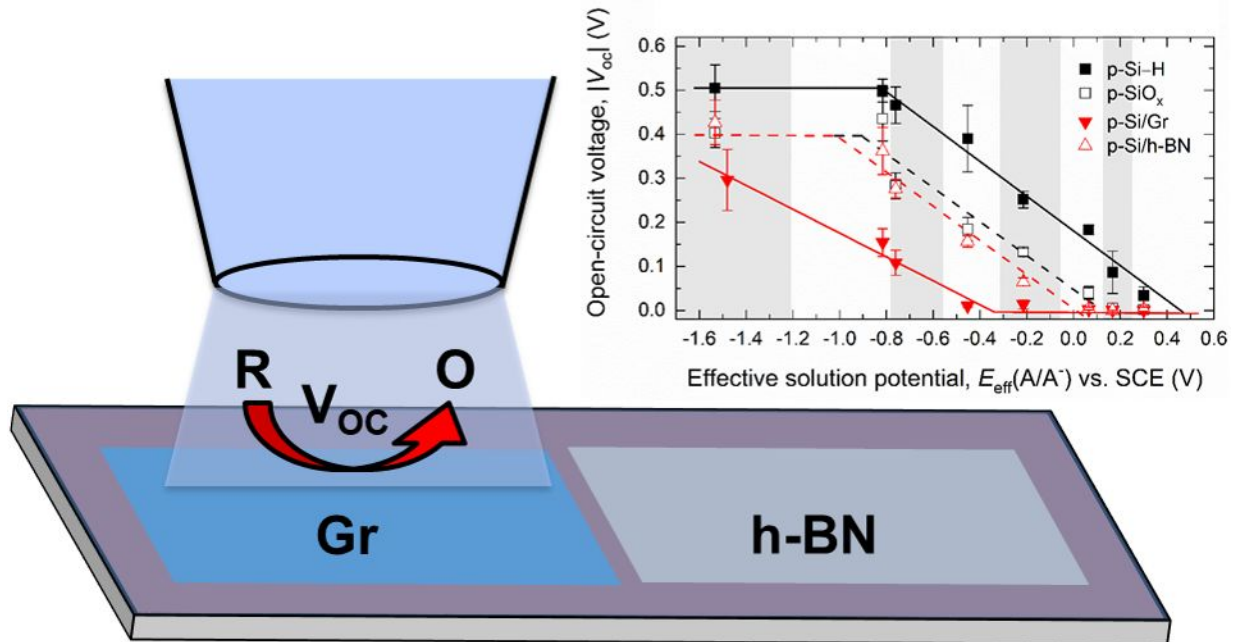
36  
37 (36) Lányi, Š.; Nádaždy, V., Scanning Probe Microscope Based Deep-Level Spectroscopy of  
38  
39 Semiconductor Films. *Ultramicroscopy* **2010**, *110*, 655-658.

40  
41 (37) Doan, Q. T.; El Hdiy, A.; Troyon, M., Three-Dimensional Simulation of Electron Beam  
42  
43 Induced Current Collected by a Nano-Contact: Diffusion and Collection Analysis. *J. Appl. Phys.*  
44  
45 **2011**, *110*, 124515.

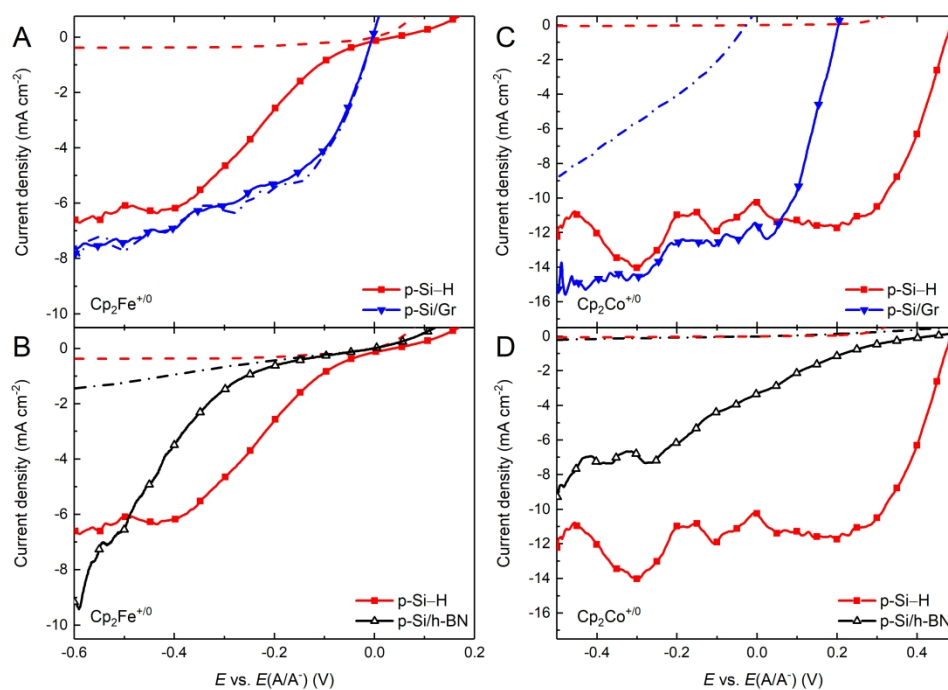
1  
2  
3 (38) Doan, Q.-T.; Hamdouni, A.; El Hdiy, A., Surface Recombination Velocity Effects on  
4 Simulated Electron Beam Induced Current Collected by a Nanoscale Electrode. *Superlattice*  
5  
6 *Microst.* **2016**, *100*, 1296-1300.  
7  
8  
9

10  
11 (39) Marchiando, J. F.; Kopanski, J. J.; Lowney, J. R., Model Database for Determining Dopant  
12 Profiles from Scanning Capacitance Microscope Measurements. *J. Vac. Sci. Technol. B* **1998**, *16*,  
13  
14 463-470.  
15  
16  
17

18  
19 (40) Marchiando, J. F.; Kopanski, J. J.; Albers, J., Limitations of the Calibration Curve Method  
20 for Determining Dopant Profiles from Scanning Capacitance Microscope Measurements. *J. Vac.*  
21  
22 *Sci. Technol. B* **2000**, *18*, 414-417.  
23  
24  
25  
26  
27  
28  
29  
30  
31  
32  
33  
34  
35  
36  
37  
38  
39  
40  
41  
42  
43  
44  
45  
46  
47  
48  
49  
50  
51  
52  
53  
54  
55  
56  
57  
58  
59  
60



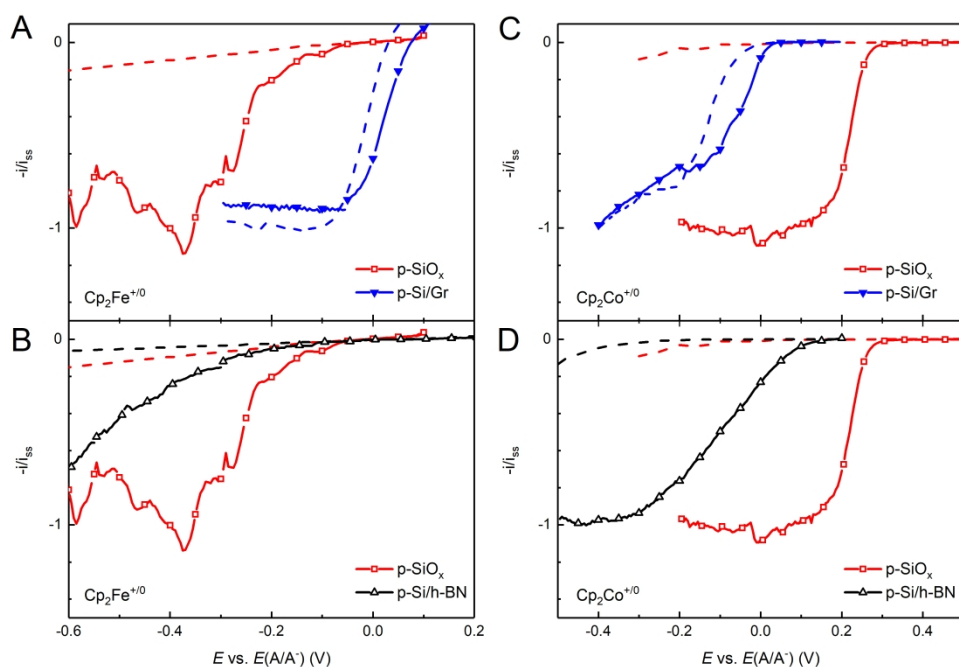




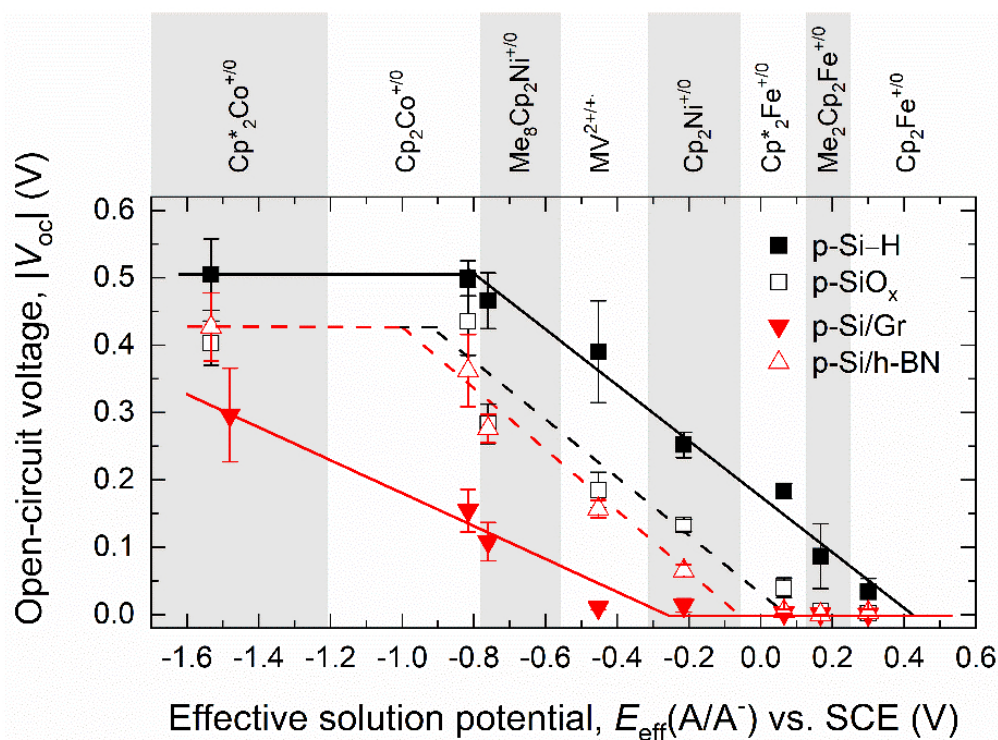
Photocurrent density vs potential ( $J$ - $E$ ) behavior of modified p-Si electrodes in contact with  $\text{Cp}_2\text{Fe}^{+/0}$  (A-B) and  $\text{Cp}_2\text{Co}^{+/0}$  (C-D), in  $\text{CH}_3\text{CN}$ -0.50 M  $\text{LiClO}_4$  under  $100 \text{ mW cm}^{-2}$  of ELH-type simulated solar illumination.

The dashed lines show scans of the same electrodes without illumination. In contact with either redox couple, the fill factor of the p-Si/h-BN electrode was substantially smaller than that of either the p-Si-H (Figure 1) or p-SiO<sub>x</sub> (Figure S7) electrodes, indicative of slow electron-transfer kinetics at the h-BN/liquid interface. In contact with  $\text{Cp}_2\text{Co}^{+/0}$ , the  $J$ - $E$  characteristics of the p-Si/Gr electrode shifted upon illumination, in addition to displaying substantially larger reverse saturation current densities than the other three types of electrodes.

177x128mm (600 x 600 DPI)

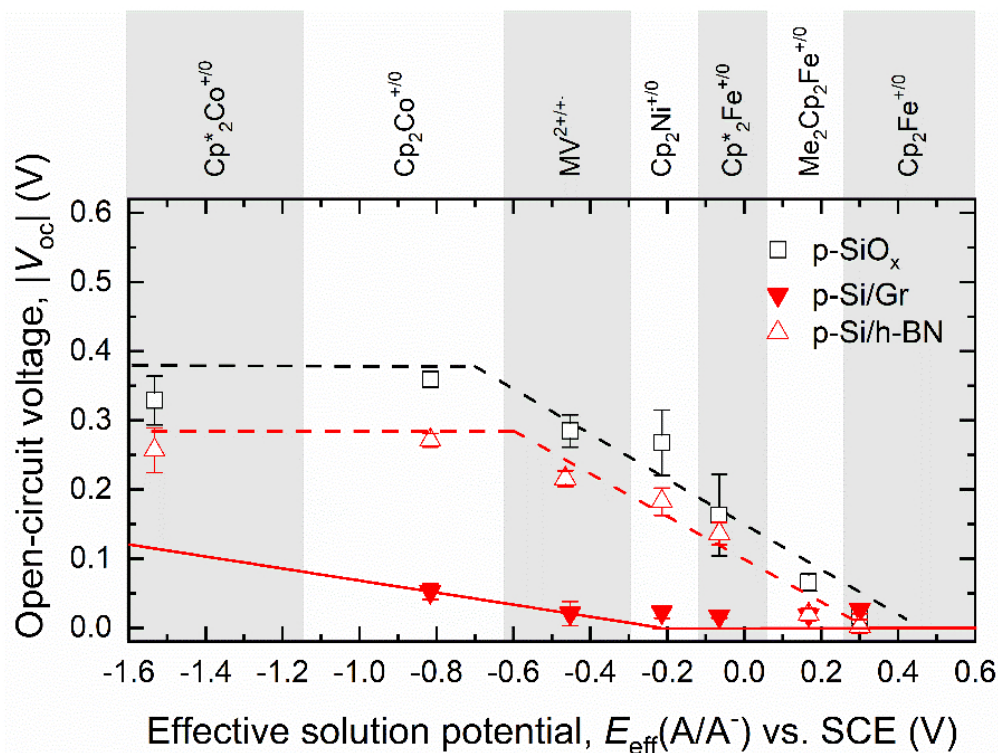


177x125mm (600 x 600 DPI)



Comparison of open-circuit voltage of macroscale p-Si-H, p-SiO<sub>x</sub>, p-Si/Gr, and p-Si/h-BN electrodes, respectively, versus the effective redox potential of various redox couples. Three regions, each highlighted by linear fits of the data therein, were identified for all samples.

105x78mm (220 x 220 DPI)



Comparison of the open-circuit voltage of p-SiO<sub>x</sub>, p-Si/Gr, and p-Si/h-BN electrodes, respectively, versus the effective potential of various redox couples, on the same SECCM electrode. Linear fits of the data have been used to highlight the different regions of behavior.

103x78mm (220 x 220 DPI)

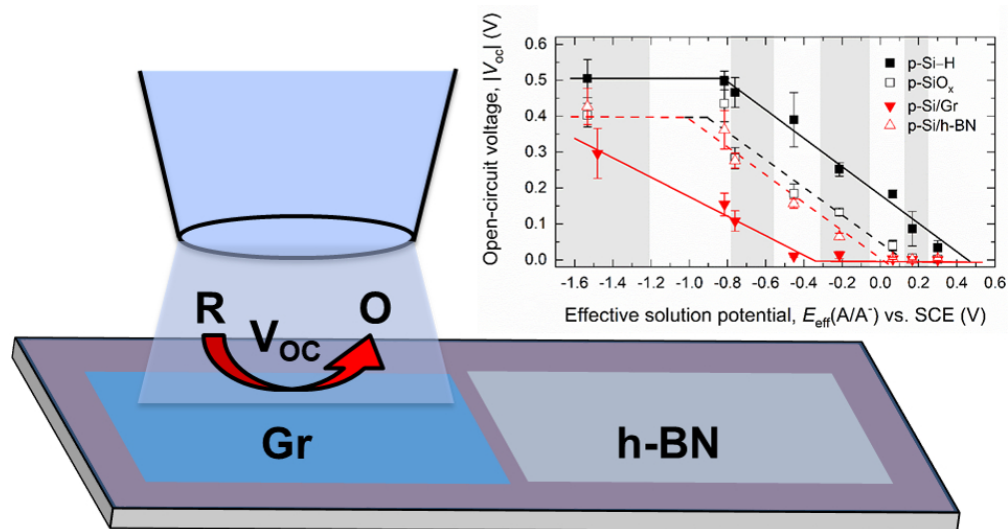


Table Of Contents Figure

161x86mm (150 x 150 DPI)